UNIVERSITY OF CALIFORNIA

Radiation Laboratory

BERKELEY, CALIFORNIA

DISCLAIMER

UCRL 1011

Nucleon-Nucleon Interaction

By

Richard Stuart Christian
B.S. (Illinois Institute of Technology) 1947

DISSERTATION

Submitted in partial satisfaction of the requirements for the degree of

DOCTOR OF PHILOSOPHY

in

Physics

in the

GRADUATE DIVISION

of the

UNIVERSITY OF CALIFORNIA

Approved:

. . . . . .

. . . . . .

. . . . . .

Committee in Charge

Deposited in the University Library. . . . . .
Date Librarian

INTRODUCTION

The purpose of the present paper is to ascertain if it is possible to determine a phenomenological description of the nucleon-nucleon interaction in terms of a potential. A further aim is to determine with what uniqueness this potential can be determined from the present experiments, particularly those at high energies. The program will be to assume a number of potential models so adjusted that they fit the low energy region and attempt to correlate the high energy scattering with the various features of each model.

It is well known that the experimental results in the low energy region can be described by an interaction potential; however, for sufficiently high energies relativistic corrections may be expected to be of major importance. Detailed scattering calculations, using a field theory, show that the use of relativistic momenta corresponds to calculating the kinematical aspects relativistically, but that the dynamical corrections depend on the specific theory employed. Scattering deduced from a field theory[1] has, in general, relativistic corrections proportional to $(v/c)^2$; for example, at 90 Mev $(v/c)^2$ is 0.05 while approximately 10 percent corrections are found by application of the Moller method to the scalar and vector meson theories[2]. These corrections do not have

---

[1] L. Rosenfeld, Nuclear Forces (Interscience Publishers, Inc., New York), Vol 2, p. 311 ff. It might appear at first sight that corrections due to spin orbit coupling are of order v/c. Actually, in a field theory calculation corrections which introduce this coupling include also a gradient of the potential (e.g., the Thomas term for the hydrogen atom) which in scattering produces an additional factor of v/c.

[2] H. Snyder and R. E. Marshak, Phys. Rev. 72, 1253 (1947).

any noticeable similarity (even as to sign) between the various field theories. Consequently, we shall attempt to fit the data disregarding any relativistic correction. We may occassionally recall, however, that an absolute choice should not be made between potentials each of which fits the experimental data to order $(v/c)^2$.

This paper shall be divided into three sections. In the first and second section we shall consider the neutron-proton and the proton-proton system, respectively. In the third section we shall summarize the apparent similarities and differences in the two interactions and consider the need for further experimental and theoretical work as well as mention possibilities for determining the neutron-neutron interaction.

SECTION I - THE NEUTRON-PROTON INTERACTION

I. Qualitative Discussion

The experimental results of the low energy region (including some derived quantities) are summarized in Table I. None of these experiments give information concerning the explicit radial dependence of the forces or of the forces in other than S-states, and, in fact even the ranges are determined only approximately. In the triplet state there is a further uncertainty in the relative central and tensor ranges. This latter uncertainty would be removed considerably if it were assumed that the magnetic moment gave a measure of the D-state admixture due to tensor forces. Unfortunately, because of uncertain relativistic corrections[3] this

---

[3] R. G. Sachs, Phys. Rev. 72, 91 (1947); H. Primakoff, Phys. Rev. 72, 118 (1947); G. Breit and I. Bloch, Phys. Rev. 72, 135 (1947).

forms an unreliable restriction. The depths of the various potentials, i.e., singlet and triplet central and triplet tensor, are, however, accurately determined for any specified combination of ranges.

The high energy experiments consist of angular measurements at 28, 40, 90 and 280 Mev and total cross sections at all these energies and at some intermediate energies. The experimental distributions are shown graphically in Figs. 1 and 2. The total cross sections are tabulated in Table II.

We propose to fit the data at 40 and 90 Mev first and then ascertain if the model or models determined will fit the remaining data. The reason for this choice is primarily because this was the first data available and it is still the most complete and experimentally reliable data. The expansion (in Legendre polynomials, $P_n(\theta)$ for the 90-Mev distribution is

$$4\pi \cdot \sigma(\theta) = \sigma\left[1 - 0.14P_1(\theta) + 0.68P_2(\theta) + 0.02P_3(\theta) + 0.11P_4(\theta)\right],$$

with an estimated error of $\pm$ 0.1 for the coefficients of $P_1(\theta)$ through $P_4(\theta)$. The most noteworthy result is the near symmetry about 90°. We have therefore assumed that the 40-Mev angular distribution, which has been determined only in the range 60°—180°, is symmetrical about 90° with the consequent expansion

$$4\pi\sigma(\theta) = \sigma(1 + 0.26P_2(\theta) + 0.02P_4(\theta)),$$

with an estimated error of $\pm$ 0.1 for the $P_2(\theta)$ and $P_4(\theta)$ coefficients.

The experimental total cross sections are tabulated in Table II. The low values for the total cross sections appear to be further corroboration of the lack of odd harmonics in scattering.

A unique analysis into phase shifts of the experimental angular distribution is impossible due to the presence of the mixture of singlet and triplet states as well as the complication of the tensor force. Nevertheless, on the simplifying assumption of scattering with no spin dependence, the 90-Mev angular distribution may be analyzed to give the order of magnitude of the phase shifts. The results of this are: S wave, $53^\circ \pm 5^\circ$; P wave, $-1^\circ \pm 1^\circ$; D wave, $5^\circ \pm 1^\circ$. Since the P and D phase shifts are so small, we may conclude that at 90 Mev the S scattering accounts for about 90 percent of the total scattering cross section. The high energy cross sections, therefore, determine the S scattering fairly unambiguously. The potentials usually considered show significant differences in S scattering above 30-40 Mev when adjusted to have the same low energy properties. The comparison then of the S wave cross sections provides one method of determining the potential shape.

The angular distribution at a particular energy yields information primarily concerning the exchange character of the forces. For example, theories such as the "charged" or "neutral" which predict large scattering in odd states may be immediately discarded as unacceptable. The low values of the high energy cross sections also favor theories without large scattering in odd states.

Finally, comparison of angular distributions at two or more high energies enables one to distinguish shape features of the

various potentials. This final comparison is a critical test of the potential shape since, while it is possible with any shape, by a proper choice of range, to fit the angular distribution at 90 Mev and the low energy data simultaneously, it will not, in general, be possible to also fit the 40-Mev angular distribution.

II. Computational Methods

Various approximate methods were employed to avoid the many tedious numerical integrations required for a comprehensive investigation of the effect of the many parameters. These are principally concerned with the integration of the radial equations to yield phase shifts or eigenvalues. For a derivation of the radial equations and the scattering amplitude with the inclusion of tensor forces see Appendix 1.

Most of the calculations were done by iteration of trial functions in the integral form of the equations. In order that this procedure might converge rapidly, it was necessary to have good initial trial functions, especially in the case of potentials with a deep hole at the origin. Suitable trial functions were provided by the WKB approximation (explicitly using one-third order Bessel functions as the asymptotic representations)[4]. This approximation has been further extended to the case of coupled equations as follows.

Let the differential equations to be solved be:

$$u'' + A(x)u + B(x)w = 0$$

$$w'' + C(x)w + B(x)u = 0 .$$

---

[4] R. E. Langer, Phys. Rev. 51, 669 (1937).

The desired representation of the solution is then

$$u = \cos n \cdot (S/S')^{\frac{1}{2}} Z_{1/3}(S)$$

$$w = \sin n \cdot (S/S')^{\frac{1}{2}} Z_{1/3}(S) .$$

Where

$$S_{\pm} = \frac{1}{2^{\frac{1}{2}}} \int_{x_1}^{x} \left\{ A + C \pm \left[(A - C)^2 + 4B^2 \right]^{\frac{1}{2}} \right\}^{\frac{1}{2}} ,$$

$$\tan n = \left[(S_{\pm}')^2 - A \right] / B ,$$

with x_1 being a turning point of $(S_{\pm}')^2$. The $+$ and $-$ signs correspond to two independent representations. The Z's are Bessel functions of order one-third. The usual phase integral condition for the bound state is replaced by the similar condition,

$$\int_{x_1}^{x_2} S' \, dx = S_n ,$$

where x_1 and x_2 are the turning points and S_n is a root of

$$(d/dS) \, (S)^{\frac{1}{2}} \left[J_{1/3}(S) + J_{-1/3}(S) \right] = 0 .$$

These representations have been found to yield close approximations to the wave functions at all energies, the S wave phase shifts being, in general, in error by less than five degrees, and the wave functions exhibiting the correct general behavior. When applied to the bound state, the phase integral condition yields potential depths that are within 10 percent of the correct value.

The bound deuteron state was numerically iterated using the variation-iteration[5] method, using as a trial function the approximate WKB functions above. Three iterations yielded an eigenvalue and wave functions with an accuracy of about one percent. The accuracy was essentially limited by the numerical methods used (intervals corresponding to one- to two-tenths of the effective range were used).

For the $^3S_1 + {}^3D_1$ scattering state, the appropriate WKB functions furnished trial functions for the coupled integral system

$$u = A \sin kx + M/h^2 \int_0^\infty G_0(kx, kx') \times \left[V_c(x')\, u(x') + 2^{3/2} \gamma V_t(x')\, w(x')\right] dx'$$

$$w = Bg_2(kx) + M/h^2 \int_0^\infty G_2(kx, kx') \times \left\{\left[V_c(x') - 2\gamma V_t(x')\right] w(x') + 2^{3/2} \gamma V_t(x') u(x')\right] dx' ,$$

where $A = 1$, $B = 0$ corresponds to the choice of the positive sign in $(S_{\pm}')^2$ and

---

5 N. Svartholm, The binding energies of the lightest atomic nuclei, University of Lund (thesis Phys. Inst. 86 pp. (1945)). J. Schwinger, Phys. Rev. 72, 742(A) (1947), and hectographed "Notes on nuclear theory," Harvard (1947).

$$A = \frac{M}{h^2 k} \int_0^\infty \cos kx' \left[V_c(x')u(x') + 2^{3/2} \gamma V_t(x')w(x') \right] dx' ,$$

$B = 1$ corresponds to the negative sign. Further,

$$G_0 (kx, kx') = (1/k) \sin kx \, \langle \cos kx \rangle$$

$$G_2 (kx, kx') = (1/k)^3 \, g_2(kx) \, \langle k^2 g_{-2} (kx) \rangle . ,$$

where $x \langle$ means the lesser of x and x', and $g_2(kx)$ and $g_{-2}(kx)$ are the regular and irregular spherical Bessel functions of order 5/2.

The potential has been written in the form

$$V(r, \sigma) = V_c(r) + \gamma S_{12} V_t(r) .$$

The iteration of the integral equations above was carried out numerically with the normalization of the trial functions so chosen that the iterated functions matched the trial functions in the region where the kernel of the integral system is largest. Three iterations for the S dominant mode (i.e., with $A = 1$, $B = 0$) and one for the D dominant mode yielded phase shifts with an accuracy of about two percent.

S phase shifts for the singlet state, and for the triplet state without tensor forces, are most quickly determined by straightforward numerical integration. For other uncoupled states such as the $^3D_2$ state the phase shift was calculated using the variational procedure with the $^3D_2$ component of the plane wave as a trial

function. The phase shift in the $^3D_3 + {}^3F_3$ state was computed using the same procedure as for the $^3S_1 + {}^3D_1$ state. One iteration yielded an accuracy of two percent.

The Born approximation was used to effect the inclusion of the angular momentum states for $\ell \geq 4$ in the scattering sum. The sum was, in general, done by actually summing the individual terms for $\ell \leq 3$, using calculated phase shifts, and adding the Born cross section from which these states had been suitably subtracted (See Appendix 1). The angular distributions so derived are accurate within two to five percent.

III. Central Forces

We shall consider in this section the results of scattering from a model which consists only of central forces since, as will be seen later, it is possible to make a state-by-state comparison of the scattering from a central force model and from one which includes tensor forces.

The details of low energy scattering will not be treated here, but, rather, the reader is referred to the review of Blatt and Jackson[6]. One result of their work is that in the expansion (the notation is explained in Table I)

$$k \cot {}^3\delta_S = -(1/{}^3a) + \tfrac{1}{2}({}^3r)k^2 - {}^3Tk^4 + \cdots\cdots$$

the shape dependent coefficient, T, is sufficiently small that below 6 Mev it can be neglected, and, in interpreting the experiments,

---

[6] J. M. Blatt, Phys. Rev. 74, 92 (1948); J. M. Blatt and J. D. Jackson, Phys. Rev. 76, 18 (1949).

the shape independent approximation may be used. The effective range in the triplet state is determined, therefore, by the approximate relation

$$(1/{}^3a) = (1/r_d)\left[1 - \tfrac{1}{2}({}^3r/r_d)\right] .$$

Substituting the experimental values from Table I, we obtain

$${}^3r = 1.68 \pm 0.10 \times 10^{-13} \text{ cm.}$$

Figure 3 is a plot of effective range versus intrinsic range for the triplet state of the various potentials.

The singlet effective range is not determined with as much precision. The determination from the total scattering cross section is best done in the region from 0 to 2 Mev, where the triplet scattering is smallest, (see Fig. 4). It may also be determined from the capture cross section, (see Table I).

To simplify the analysis of the high energy data, it is convenient (and reasonable) to assume exact symmetry of scattering about 90°. This means that the potential is assumed to be zero in odd parity states. The experimental results are actually compatible with a small repulsive potential in odd states, but this shall be considered as a small perturbation which will not essentially alter any of the following conclusions. The factor $\frac{1}{2}(1 + P_x)$ will, therefore, be included as a factor in the potential and will have as one consequence that the total cross section computed for any radial dependence will be the minimum possible over any other choice of exchange dependence. The main

effect of any admissible odd wave phase shifts is the interference with the large S wave phase shift, which is in evidence only in the angular distribution, and its actual effect on the total cross section is negligible.

In order to compare different potential shapes, the effective range has been taken as a common parameter. For example, we have plotted (Fig. 5) the S wave phase shift at 90 Mev for the various potentials versus the effective range. This device insures similar low energy behavior for the same abscissa.

In Fig. 6 are plots at 90 Mev, for the various potentials, of the total cross section and of 4π times the differential cross section for scattering at 90° and 180° as functions of the effective range on the assumption of no odd parity interaction. For the plots of complete total cross section, i.e., the sum of triplet and singlet scattering, it is necessary to make some choice of a singlet range corresponding to a particular triplet range. The low energy region implies only loose restrictions on the singlet range; we may, therefore, choose the singlet range so that the singlet and triplet intrinsic ranges are equal. The results for the complete cross sections are also shown in Fig. 6. From these plots it is possible to make further limitations on the allowable triplet ranges by a comparison with the experimental values of $\sigma(180^\circ)/\sigma(90^\circ)$.

With the Yukawa or exponential potential, a range adjusted for the 90-Mev ratio predicts a 40-Mev ratio within the experimental limits. However, with the square well potential,

the range required at 40 Mev is considerably larger than that required at 90 Mev. This difference in behavior results primarily from the more rapid decrease in $\sigma(90^{\circ})$ with energy increase for the "cut-off" potential than for the "long-tailed" potentials. This, in turn, can be interpreted in terms of the destructive interference between the S and D waves at 90°. In detail, the S wave phase shift decreases more rapidly (as a function of energy) for the cut-off potentials (Fig. 7). Further the D wave phase shift is nearly a linearly increasing function of energy for the long-tailed potentials, while the increase with energy is much more rapid for the cut-off potentials (Fig. 8).

For potentials which have a "deep hole" at the origin (e.g., the Yukawa and exponential), the long-tail is necessary to give a sufficiently long effective range. However, as the energy increases the contributions to the S wave phase shift come from regions closer to the origin, and, consequently, at high energies the deep hole (and, therefore, long-tailed) potentials yield larger phase shifts than the cut-off potentials (e.g., the square well or Gauss potentials). These remarks are further illustrated by reference to Figs. 5 and 7.

While it is impossible to define the limits of the singlet effective range with any accuracy, for ${}^3r \lesssim 1.7 \times 10^{-13}$ cm, the best fits for the angular distribution are obtained with the singlet effective range between $2.5 - 3.0 \times 10^{-13}$ cm.

The complete angular distribution is shown in Figs. 9 and 10, for the Yukawa and exponential potentials with ranges chosen such that they are both good fits of the angular distribution at

90 Mev. From this the superiority of the Yukawa angular distribution at 40 Mev is apparent. The total cross sections, however, are in much better agreement with the exponential potential.

The only partial waves contributing appreciably to the cross sections are the S and D waves, consequently, the angular distribution can be expanded in terms of Legendre polynomials P_o, P_2, and P_4. The coefficient of P_o is identical with the total cross section, that of P_2 arises primarily from the interference between the S and D states, and that of P_4 arises primarily from the combinations of the various D states. These coefficients allow a rapid comparison of theory and experiment and are therefore tabulated in Table III for all models mentioned explicitly.

If we consider the Yukawa and exponential potentials of Figs. 9 and 10, we see that the only discrepancy with the experimental values of the coefficients occurs in the magnitude of the P_4 coefficient which is perhaps a factor of two to three too large. This is manifested in the angular distribution by a theoretical prediction that is somewhat too flat in the region about 90°.

Figure 9 and Table III show the effect of adding a small repulsive potential in the odd parity states. This modification may be expressed by a potential factor, $(1 - a + aP_x)$. The best fit for this type of exchange interaction is $a = 0.55 \pm 0.05$.

i.e. makes more than ordinary exchange force

The large odd state potentials in the singlet state required by the symmetrical theory produces far too much exchange scattering for any potentials with a tail and a range compatible

with low energy scattering. For cut-off potentials such as the square well, the observed ratio $\sigma(180^\circ)/\sigma(90^\circ)$ may be fitted at 90 Mev with a range of $1.7 - 1.8 \times 10^{-13}$ cm; however, at 40 Mev, a fit to $\sigma(180^\circ)/\sigma(90^\circ)$ would require a range longer than 2.0×10^{-13} cm. Furthermore, in these latter cases the shape of the predicted angular distribution is not similar to the experimental results for small angle scattering. The symmetrical theory can, therefore, be ruled out for central forces.

IV. Tensor Forces

A. The Bound State and Low Energy Scattering

The existence of the deuteron quadrupole moment requires the inclusion of a tensor potential in the neutron-proton interaction. We consider first the case where the radial dependence is chosen the same for both the central and tensor potentials. The extreme cases of long-tailed and cut-off potentials are exemplified by the Yukawa and square well, respectively. Calculations of the quadrupole moment have been made for these potentials as a function of range and tensor depth with the central depth adjusted to give the correct binding energy. The results are presented graphically in Figs. 11-13.

The calculations of Rarita and Schwinger[7] have shown that at least for the choice of a square potential, there is only slight modification of the low energy scattering properties upon the introduction of tensor forces. Such behavior can be expected for more general potential shapes with ranges shorter than the

---

[7] W. Rarita and J. Schwinger, Phys. Rev. 59, 436 (1941).

deuteron radius since the S wave component is determined primarily from the boundary conditions at the origin and asymptotically[8].

We can put these arguments on a quantitative basis by the consideration of an "equivalent central potential," "V(r)". For the potential $V(r) = V_c(r) + \sigma S_{12} V_t(r)$, the equivalent central potential for the S wave is

$$"V(r)" = V_c(r) + 2^{3/2} \sigma V_t(r) \cdot R(r) ,$$

where R(r) is the ratio of the D wave to the S wave. R(r) will be, in general, a slowly varying function of the energy (at least in the region where the potential is large). Its form may then be estimated from considerations of the bound state solutions. It is found then that R(r) is zero at the origin, increases to a maximum value (about 0.2 or 0.3) somewhere between the maximum of the S wave radial function and the tensor force range, and decreases a symptotically to a small value (somewhere under 0.1). Then if we consider the ratio of the equivalent potential "V(r)" to the central potential $V_c(r)$ (the latter adjusted to give binding by itself), we would find the ratio to be less than unity at the origin, greater than unity in the neighborhood of the range, and again less than unity asymptotically. Thus the equivalent potential will be shallower at the origin and asymptotically, and will be deeper in the neighborhood of the tensor range.

This can be further illustrated in terms of the WKB approximation. In this approximation, R(r) is independent of energy

---

[8] W. Hefner and R. Peierls, Proc. Roy. Soc. 181, 43 (1942).

and decreases asymptotically to zero. The equivalent potential in this approximation is

$$"V" = V_c - \sigma V_t - \frac{3}{r^2} + \left[\left(\sigma V_t + \frac{3}{r^2}\right)^2 + 8(\sigma V_t)^2\right]^{\frac{1}{2}} .$$

Since the centrifugal potential is usually large compared to the tensor potential, this may be simplified to

$$"V" = V_c + \frac{4}{3}(\sigma r V_t)^2 ,$$

which is clearly in agreement with the preceding remarks.

The analysis of the low energy scattering is again conveniently carried out in terms of the expansion of the phase shift in powers of the energy[9]. Since the shape-independent approximation is valid for Yukawa ranges less than 1.4×10^{-13} cm and for all square well ranges considered, the effective range is essentially determined from the triplet scattering length. (The explicit value of the shape-dependent coefficient as well as the effective ranges are shown in Table IV for a number of cases.) We have chosen, therefore, in order to relate the scattering characteristics of a potential with its ability to produce a quadrupole moment, to plot $1/\sigma$ versus the scattering length (Fig. 14) with the range indicated parametrically along the curves. From this plot we can conclude that with the accepted value of the scattering length, the proportion of tensor potential must be quite large, the actual amount being lower for the long-tailed potential.

---

[9] R. Christian, Phys. Rev. 75, 1675 (1949).

The low energy constants for the case in which the tensor force range is increased relative to the central force range are given in Table IV and Fig. 15. From the equivalent potential we see that the main effect is to increase the long-tailed character of the potential. This is evident by the decrease in the percentage D state and by the increase in the shape-dependent coefficient.

B. High Energy Scattering (40 and 90 Mev)

We will attempt in the next paragraphs to gain a qualitative understanding of the relation between central and tensor scattering. Then we will consider the result of various models, the calculations being carried out by the methods previously described.

As in the case of central forces we must adjust the ranges so that only the S and D partial waves contribute to the cross section. We would then expect that if the tensor force were a weak effect we could add the tensor scattering which would be present in Born approximation. Actually, as we have seen, the tensor force is far from weak and the approximation can only be expected to give the general trend. The characteristic peaking of the Born approximation cross section around 45 and 135° (the exact angle depending upon the model, range, and energy with a maximum occurring roughly where $2kR \sin \theta/2 \sim 1$) is, in fact, the type of correction needed to explain the discrepancy between the shapes of the experimental curves and the central force curves shown in Figs. 9 and 10, i.e., such a correction could convert the U-shaped central force curves into the more V-shaped experimental curves.

For a somewhat more detailed comparison we will again use the WKB approximation to approximate the equivalent central potentials, "V_L^J," for each of the states L and J, with the result

$$"V_o^{\,1}" = V_c - \gamma V_t - \frac{3}{r^2} + \left[\left(\frac{3}{r^2} + \gamma V_t\right)^2 + 8(\gamma V_t)^2\right]^{\frac{1}{2}}$$

$$\approx V_c + \frac{4}{3}(\gamma r V_t)^2 \quad ,$$

$$"V_2^{\,1}" = V_c - \gamma V_t - \frac{3}{r^2} - \left[\left(\frac{3}{r^2} + \gamma V_t\right)^2 + 8(\gamma V_t)^2\right]^{\frac{1}{2}}$$

$$\approx V_c - 2\gamma V_t + \frac{4}{3}(\gamma r V_t)^2 - \frac{6}{r^2} \quad ,$$

$$"V_2^{\,2}" = V_c + .2\gamma V_t - \frac{6}{r^2} \quad ,$$

$$"V_2^{\,3}" = V_c - \gamma V_t - \frac{13}{r^2} + \left[\left(\frac{7}{r^2} + \frac{3}{7}\gamma V_t\right)^2 + 3\left(\frac{12}{7}V_t\right)^2\right]^{\frac{1}{2}}$$

$$\approx V_c - \frac{4}{7}\gamma V_t + \frac{3}{14}\left(\frac{12}{7}\right)^2(\gamma r V_t)^2 - \frac{6}{r^2} \quad .$$

In the approximation where we neglect the asymptotic amplitude of the coupled mode, as above, in the evaluation of the phase shifts there will be no difference between states of different magnetic quantum number, m_s ; however, the WKB approximation yields

angular distributions which agree with the results of a more accurate calculation within 10 to 20 percent.

As can be expected on the basis of the "equivalent potentials", there is only a small difference in the total scattering from the $^3S_1$ state. Further, we can summarize the behavior of the various D states in the following: ($^3D_1$) Increasing the tensor depth (i.e., γ) decreases the equivalent potential and for strong tensor forces the resulting potential will be strongly repulsive. ($^3D_2$) Increasing γ increases the potential depth to such an extent that for $\gamma \gtrsim 1$, the depth is three to four times as deep as the depth on the central force model. ($^3D_3$) The potential decreases for increasing γ such that for $\gamma \gtrsim 1$ the potential will be just barely repulsive. (Approximately the same effects can be achieved by increasing the tensor range instead of the depth.)

To illustrate these remarks we will consider the high energy scattering from two extreme examples (calculated exactly): (1) The central and tensor depth are approximately equal with the square well radial dependence of range 2.7×10^{-13} cm; (2) the tensor depth accounts for practically all the binding with a Yukawa dependence and range of 1.2×10^{-13} cm. In Table V we have summarized the contribution of each state to the total cross section and indicated the sign of the phase shift (i.e., the average over m_s). The results of the central force model with the same range and radial dependences are included for comparison.

Utilizing this comparison between the tensor and central force models we can conclude that the potential must be long-tailed in order to maintain the relatively large scattering in the D state

at 40 Mev without excessively large scattering in the D state at 90 Mev. Cut-off (e.g., square and Gauss) potentials where the tensor force has nearly the same range as the central forces are, therefore, unsuitable. An addition of a long shallow tail ($5 - 6 \times 10^{-13}$ cm) to the square well is required in the central force case to fit with the 40- and 90-Mev scattering and would, therefore, also be required for tensor forces. Potentials formed by the addition of such long-tails would seem to be indistinguishable from naturally long-tailed potentials such as the exponential or the Yukawa potential.

The results of using the Yukawa and exponential radial dependences (see Figs. 16-18) indicate that the addition of tensor forces causes only relatively small changes in the scattering. The best fits of the angular distribution require slightly longer ranges than for the purely tensor model. A detailed comparison, using the Legendre coefficients, shows that the $P_4(\theta)$ component is reduced in the tensor model. It is this decrease which allows considerably better fits of the angular distribution and is therefore evidence for the presence of tensor forces in scattering. The total cross section is increased, however, approximately 10 percent with the addition of tensor forces so that the agreement with the experimental value of the total cross section is poorer.

The same situation holds for the tensor model as for the central model regarding the intercomparison of the Yukawa and exponential potentials. That is, the Yukawa potential fits the angular distributions at both 40 and 90 Mev noticeably better, however the total cross section is 20 to 30 percent too high. The

total cross section with the exponential potential is only 10 to 15 percent too high. Since the long-tail, which is necessary to fit the angular distribution, forces the potentials considered here to have a deep hole also and consequently high cross section, it would seem that an essentially more complicated radial dependence would be necessary to fit the experimental results more closely.

The exchange character found necessary for the central force model is also valid, in the main, for the tensor force model (see Table III). As an example of spin dependent exchange dependence we have considered the case when the central force has a $\frac{1}{2}(1 + Px)$ exchange dependence and the tensor force exchange dependence was of the form $(1 - a + aPx)$. This does not produce as large asymmetries in the angular distribution as when $(1 - a + aPx)$ is taken as a factor of both the central and tensor potential. The restriction on the magnitude of a now arises mainly from the increase in the total cross section. These limits are estimated to be $a \simeq 0.6 \pm 0.1$.

The principal change in the high energy scattering with increase in tensor range, is according to the WKB arguments, similar to an increase in the long-tailed character of the potential. The high energy scattering results are shown in Fig. 19 for the cases listed in Table IV. There is an increase in scattering from the higher states which may be interpreted as the increase in the long-tailed character or alternatively as showing that the characteristic Born approximation tensor peaking is displaced to smaller angles.

V. Additional N-P Experiment

The angular distribution has been measured at 27.2 and 280 Mev (see Figs. 1 and 20). Total cross sections have been measured at various energies extending from 20 to 270 Mev (see Table II).

The comparison of the 27.2 Mev data with the Yukawa tensor model is shown in Fig. 20. From this we see that again as at 40 Mev the predicted angular distribution is somewhat flatter than the experimental data. The accuracy of the experiment is not sufficient, however, to definitely exclude this model. It may be noted by reference to Fig. 6 that the exponential radial form would predict an even more isotropic distribution and can therefore probably be eliminated. The cross section predicted for the Yukawa model is 0.344 barns as compared with the experimental value of 0.36 ± 0.03 barns.

The comparison of the 280 Mev data with the Yukawa tensor model is shown in Fig. 17. The agreement is very good, which would not have been the case if the exponential model (or any of the purely central force models) had been used. A striking confirmation of the general properties of the Yukawa model is thus found from the high energy data.

Next we wish to note that all of the models seriously considered (because of the smallness of the odd state potentials) predict nearly isotropic distribution at 14 Mev in agreement with the recent experiments of Barschall and Taschek[10] who find isotropy within their statistical accuracy of six percent.

---

[10] H. H. Barschall and R. F. Taschek, Phys. Rev. 75, 1819 (1949).

SECTION II - THE PROTON-PROTON INTERACTION

I. Introduction

In this section we will be concerned with the proton-proton scattering data at 32 Mev[11, 12] and 340 Mev[13]. The success that was obtained in the n-p system would seem to be sufficient grounds for expecting that p-p scattering would likewise be interpretable by means of static potentials. In fact we might be tempted to predict the p-p nuclear potential from our knowledge of the n-p potential as determined by the high energy scattering. This prediction could be made either on the hypothesis that the nuclear potential is charge independent (i.e., depends only upon whether the two particles are in a singlet or triplet spin state), or in terms of an attempt to explain the saturation of nuclear forces.

If we were to follow the first assumption (the so-called charge symmetry hypothesis) there would be no free parameters entering the p-p theory, since the results of the n-p experiments are quite definite. For both singlet and triplet states these experiments show that there are no (or very small) odd parity forces. Therefore on the basis of charge symmetry one might expect that the n-p and p-p scattering would be quite similar. This is in obvious disagreement with the experimental results as is seen in Fig. 21.

---

11 W. K. H. Panofsky and F. Fillmore, Phys. Rev. 79, 57 (1950).

12 Cork, Johnston and Richman, Phys. Rev. 79, 71 (1950).

13 O. Chamberlain and C. Wiegand, Phys. Rev. 79, 81 (1950).

In order to better understand the prediction of the charge symmetric theory we must consider in more detail the fundamental differences between n-p and p-p scattering. Firstly, for 32-Mev protons the Coulomb repulsion is dominant in the scattering at angles less than 20°. Between 20° and 40° or 50° the angular variation is governed by the nuclear-Coulomb interference terms. The remaining region around 90° is virtually the same as for simple nuclear scattering. Secondly, the p-p system, being composed of identical particles obeying the exclusion principle, has fewer states than the n-p system. Specifically only even parity singlet states and odd parity triplet states can be present. Thus scattering occurs only in ^1S, ^3P, ^1D, ^3F, ... states, and the charge symmetric theory predicts the virtual absence of triplet scattering. The n-p system, on the contrary, has scattering from both singlet and triplet even parity states so that a direct comparison must be justified. In order to learn what part of the complete n-p scattering is singlet scattering we must recall that in order to lead to the low total n-p cross section the singlet range must be greater than 2×10^{-13} cm. This gives an angular distribution for the singlet cross section that has an even higher ratio of $\sigma(180^{\circ})/\sigma(90^{\circ})$ than the complete scattering from both states, making a direct comparison of the relative angular variation of the complete n-p and p-p cross sections possible in the region from 50° to 90°. Thus the 32-Mev p-p results show that the charge symmetry hypothesis is untenable.

Alternatively we could attempt to predict the p-p scattering by directing our attention to the phenomenon of the saturation of

nuclear forces. The n-p experiments rule out the possibility of n-p repulsive forces of anything like the magnitude required to explain saturation. The low energy experiments show that the singlet p-p forces are attractive. Thus the only remaining way for the p-p forces to lead to saturation would be the existence of strong repulsive forces in the triplet state. Since the triplet scattering amplitude is antisymmetric, the scattering from a central triplet potential is zero at 90°. Hence such repulsive forces would lead to an angular cross section rising even more rapidly on either side of 90° than that predicted by the charge symmetric theory and are conclusively excluded by the data.

Thus both the hypothesis of the charge independence of nuclear forces and the possibility of strong repulsive forces in the triplet p-p state such as seem to be required for the saturation of nuclear forces are already disallowed by the p-p scattering at 32 Mev. The 340-Mev scattering is even more strikingly anomalous (see Fig. 21). The experiments indicate a nearly spherically symmetric distribution over the range from 41° to 90° having an absolute magnitude that is twice the maximum possible for S wave scattering alone. Since the n-p scattering at 280 Mev was in good agreement with a non-relativistic potential model it is difficult to accept this as a relativistic effect. Again both charge symmetry and repulsive triplet forces would lead to scattering strongly peaked at 0° and 180° and an order of magnitude lower in value at 90° than the observed p-p cross section, and are conclusively disproved. This scattering is superficially similar to classical hard sphere scattering. However, since the wave-length of 340 Mev protons

is only three or four times shorter than the range of the attractive region that must surround and include such a sphere in order to explain the low energy results, the sphere cannot be made large enough to give classical hard sphere scattering at this energy. This point is discussed in more detail below.

In spite of the surprising divergence of the observed p-p scattering from that which had been expected previous to the experiments, it has proved possible to reconcile all the existing data with the scattering predicted from a static nuclear potential. This model consists of a shallow singlet potential and a highly singular triplet tensor potential. The main section of this paper is concerned with justifying this model.

In view of the apparently fundamental differences between the expected and the observed p-p scattering, and the various complicating factors in the analysis of the data, we have devoted the first part of this section to a more or less qualitative discussion of p-p scattering. In this section we will give typical results for various potential models but will not discuss which radial dependence is to be preferred. Rather we wish to emphasize the salient features in the analysis in order to furnish a basis for understanding the calculations which follow in Part III.

II. Qualitative Discussion

It has been shown by many authors that the experiments below 14 Mev are compatiable with S wave scattering alone[14] and

[14] Yost, Wheeler and Breit, Phys. Rev. 49, 174 (1936). Breit, Condon and Present, Phys. Rev. 50, 825 (1936). Breit, Thaxton and Eisenbud, Phys. Rev. 55, 1018 (1939). Hoisington, Share and Breit, Phys. Rev. 56, 884 (1939). H. M. Thaxton and L. E. Hoisington, Phys. Rev. 56, 1194 (1939).

that these experiments have determined only the scattering length and effective range[15]. This indicates that no one of the radial forms usually assumed is to be preferred. It need hardly be emphasized that the low energy experiments give little information concerning the interactions in states of higher angular momentum (especially the P state) other than putting upper limits on the magnitudes of the interactions in these states.

The n-p experiments at 40 Mev have shown that there is scattering in the D state and little scattering in the P state, and that the magnitudes of these interactions could be determined. It was therefore expected that since the range of forces for the p-p system is comparable, the scattering would likewise occur primarily in the S, P and D states.

It was observed immediately, as has been pointed out in the experimental papers[11, 12], that the data were in good agreement with that predicted by S wave scattering alone. This is in definite disagreement with the scattering predicted by the usual potential models. The reason is that the S state interaction completely specifies the entire singlet interaction, and in particular the effective range is so long that the D wave predicted at this energy is incompatible with the experimental results. (It would of course be possible to choose a potential that would give only S scattering at 32 Mev, but the effective range of such a

---

15 J. Schwinger, Phys. Rev. 72, 742A (1947). J. M. Blatt and J. D. Jackson, Phys. Rev. 76, 18 (1949), Rev. Mod. Phys. 22, 77 (1950). H. A. Bethe, Phys. Rev. 76, 38 (1949).

potential would then be much too short to fit the low energy region.)

If we consider in detail the predictions of the usual models we find that even for the most cut-off potential (the square well) the D phase shift is already too large (0.77°), and as is to be expected the more long-tailed Yukawa potential has an even larger D phase shift (1.4°). The adverse effect of such D phase shifts on the angular distribution can be readily seen by reference to the second panel of Fig. 22. The origin of this effect is destructive interference between S- and D-wave scattering in the region around 90°. This interference term is proportional to $\sin\delta_S \sin\delta_D \cos(\delta_S - \delta_D)P_2$. ($P_2(\cos\theta) = \frac{3}{2}\cos^2\theta - \frac{1}{2}$.) The usual models predict positive values for δ_S and δ_D, so that this term has a minimum at 90° as is observed in the n-p scattering but not in the p-p case. (Figure 22 also demonstrates that the Coulomb scattering has little effect in the region from 50° to 90° and hence cannot alter this conclusion.)

The central triplet scattering amplitude being anti-symmetric leads to a cross section that is zero at 90°, and since there is no interference with the singlet state it can only add to the rise away from 90°. Therefore scattering in this state will increase the discrepancy between the predictions made from the central force model and the experiments. Alternatively we can see this directly from the fact that the P scattering is proportional to $\sin^2\delta_P \cos^2\theta$, showing that the $\cos^2\theta$ term must have a positive coefficient. These effects are illustrated in the third panel of Fig. 22.

In order to explain the 32-Mev data, we require a model that would predict essentially spherically symmetric scattering in the absence of the Coulomb field. We have already seen that central force scattering predicted by monatonically decreasing potential models of the usual radial form is in qualitative disagreement with experiment. Conceivably a more complicated radial dependence, such as a repulsive lip on a square well, could lead to negligible D phase shifts at 32 Mev. Attempts to build such models have been unsuccessful because they have effective ranges too short to fit the low energy data. In view of the straightforward interpretation of the n-p scattering and the inherent difficulty of using such a model to fit the 350-Mev data, it did not appear profitable to pursue such models any further.

The remaining alternative, within the framework of the potential picture, is the possibility that the D wave is masked by the scattering from tensor forces in the triplet state. A favorable result is predicted by the use of the Born approximation to compute the scattering (see Fig. 23). (The Born approximation is valid for the P waves since the centrifugal barrier reduces the effect of the nuclear potential to a small perturbation.) The scattering computed this way is peaked at 90° and hence can add to the singlet cross section, which dips at 90°, to give an almost flat nuclear cross section. When the Coulomb effects are included the resulting angular distribution is quite similar to S wave scattering (see Fig. 24). Thus a proper choice of range and depth for the tensor potential can lead to agreement with the experiments.

(An alternative way of understanding why the scattering can have a finite value at 90° even though it takes place in odd states is that the tensor force brings about a change in angular momentum, and tesseral harmonics other than the Legendre polynomials enter into the scattering amplitude. We can then see that the presence of $Y_1^1(\theta, \phi) = e^{i\phi} \sin\theta$ in addition to $Y_1^0(\theta, \phi) = \cos\theta$ leads to terms with a $\sin^2\theta$ symmetry which when added to the $\cos^2\theta$ symmetry terms in the singlet scattering could lead to a flat nuclear cross section.)

The 340-Mev data will first be analyzed independently of the 32-Mev data. The two models so derived will then be compared and reconciled. In order to further emphasize the anomalous nature of the high energy scattering, we note that if we assumed (arbitrarily) that there were no interactions in other than S states the predicted cross section would be spherically symmetric but ten or more times too small. (Recall that even the maximum possible S wave cross section is only one-half the measured value.) The Coulomb scattering falls to the value of the nuclear cross section between 6° and 7° so that Coulomb effects will be unimportant beyond about 12° and have been neglected in our analysis.

To analyze the situation in somewhat more detail we shall first consider the scattering that would result from the singlet state (since in this state the potential is completely specified by the assumption of a particular radial form). At 350 Mev the Born approximation is valid for central scattering and predicts the strong forward maximum illustrated in Fig. 25. Alternatively we may view the problem in terms of a partial wave decomposition.

Only the even Legendre polynomials comprise the scattering amplitude. The even polynomials are all 1 at 0° and 180° and alternate in sign at 90° (e.g., $P_0(90^\circ) = 1$, $P_2(90^\circ) = -0.5$, $P_4(90^\circ) = 0.375$, ...). Scattering by the usual monatonic potential models predicts that all phase shifts will have the same sign, so that there is constructive interference at 0° and 180° and destructive interference at 90°, giving a characteristic peaking of the angular distribution.

In order to obtain a flat cross section it would be necessary to require that the sine of the phase shifts of even parity alternate in sign with increasing ℓ, resulting in a singlet cross section peaked at 90°. Then if this cross section were added to the central triplet cross section (which is always zero at 90°) a flat cross section would result. It does not appear possible, however, to find a singlet potential that will fit the scattering in the low energy region while at the same time predicting the required alternation in sign of the high energy phase shifts.

Before turning to tensor models we will first consider the so-called hard sphere scattering. To give this type of scattering phase shifts from high angular momentum states must be involved some of which must be greater than 180° in order to change the signs of the sines. One can estimate by reference to Fig. 7 of Mott and Massey[16] that in order to give agreement with the experiments the phase shifts must be large for angular momentum states up to $\ell = 20$. At this wave-length of 0.5×10^{-13} cm it might

---

16 N. F. Mott and H. S. W. Massey, THE THEORY OF ATOMIC COLLISIONS, (Oxford University Press, London, second edition) pp. 38-40.

appear that a repulsive core in the central potential would give this result. An attempt was made using Morse potentials to find a model that would predict hard sphere scattering at 340 Mev. These potentials consisted of a repulsive core surrounded by an attractive region adjusted to give the correct scattering behavior at low energies. It is found that even in the limiting case where the repulsive core becomes infinitely high, the low energy experiments require the radius of the core to be so short (1.2×10^{-13} cm) that at 340 Mev only the lowest angular momentum states are involved in the scattering (for $\ell > 6$, $\delta_\ell < 0.1^\circ$). It therefore appears that the effective range of the potential well will limit the radius of any potential to such an extent that hard sphere scattering cannot result. Alternatively we may note that even if we do not fit the low energy scattering, the absolute value of the cross section predicted by hard sphere scattering would be much too large. This can easily be seen by noting that the experimental value is $2\,\lambda\!\!\!^{-2}$ per steradian while that predicted by hard sphere scatterint must be of the order of $2(20\lambda\!\!\!^{-})^2$ since the extent of the hard core must be approximately $20\lambda\!\!\!^{-}$.

Again we must appeal to the tensor force in order to obtain agreement with the experimental data. In fact, if we recall that at 32 Mev we needed to add a triplet cross section that was peaked around 90° in order to mask the minimum in the singlet scattering we see that the situation at 350 Mev is very similar. We can again use the tensor force to obtain agreement, for in Born approximation scattering depends only on the combination kR where k is the wave number and R the range of the potential. That is,

to produce the same scattering at a higher energy we need only contract the range by a factor that is the square root of the energy ratio, and adjust the depth to give the desired absolute magnitude to the scattering.

We therefore have indications of a tensor potential at both 32 and 350 Mev, and need only show that the requirements for the two cases are compatible. As the energy changes different regions of the potential will play the more dominant role. For example, at 32 Mev the potential region at distances of the order of 3 to 4 x 10^{-13} cm is most important while at 340 Mev the potential region at distances of the order of 1 x 10^{-13} cm has become important. By adjusting the range and depth of a tensor potential of any given radial form the predictions may be made to fit the 32 Mev experimental data. However, at 340 Mev the P wave protons are able to explore the potential into considerably shorter distances and it is necessary to have a strong interaction in this region in order to explain the very high 340-Mev cross section. The tensor scattering calculated for a singular potential in Born approximation as illustrated in Fig. 23 illustrates these remarks. From the foregoing curves we can also see that an appreciable fraction of the 32-Mev scattering must be explained in terms of tensor forces if we wish to obtain agreement with the high energy data. These curves further show that the tensor potential would probably have little effect below 10 Mev as the scattering amounts to less than one percent of the total scattering.

III. Calculations

A. Methods

The singlet scattering from a potential of given radial form depending on two parameters is completely specified by the scattering length and effective range, which are determined by the scattering below 10 Mev. The general method of determining these parameters for a given radial dependence is discussed in detail by Blatt and Jackson[15]. The S scattering due to the nuclear potential alone at higher energies was calculated by direct numerical integration of the radial wave equation giving the S phase shift. The true S phase shift (in the presence of the Coulomb field) was then obtained by treating the Coulomb field as a perturbation according to the method of Chew and Goldberger[17]. The corrections amounted to approximately one degree or less. The D phase shift was calculated in Born approximation considering only the nuclear forces. (This method was checked by numerical integration in the case of the Yukawa potential, corrected for the Coulomb field as above. The results at 32 Mev: 1.33° for the Born approximation, 1.45° for the exact nuclear calculation, 1.40° with the Coulomb correction were assumed to be a satisfactory check.) Higher waves than the D were found to be negligible at 32 Mev.

As was shown in part II, it was not necessary to calculate any odd parity phase shifts due to central forces, but the tensor scattering was required. This was calculated with the exact values of the complex phase shifts, $\delta_l^{Jm_s}$, which enter into

---

17 G. F. Chew and M. L. Goldberger, Phys. Rev. 75, 1637 (1949).

the tensor scattering. The result was in good agreement with that predicted by the Born approximation. There is a slight tendency for the Born approximation to predict somewhat larger angular variations than are found in the more exact calculations. This can readily be understood in terms of the higher approximations of the Born approximation for then the scattering amplitude entering into each successive iteration (or each successive collision) is less well collimated than that entering the previous iteration, due to the scattering that occurs. A further small difference between the exact and the Born calculations occurs in the absolute magnitude, a tensor force taken with a positive sign (i.e., same sign as for the deuteron) always has less scattering in the exact calculation while the tensor force taken with a negative sign always has more scattering. A comparison between the exact predictions using the two signs and with the result of the Born approximation is afforded by reference to Figs. 26 and 27.

The phase shifts arising from the coupled states entering the exact calculations were carried out by iteration (in the manner described in Section I, Part II) after they had been cast in the form of coupled integral equations. In the case of the uncoupled states any of the methods usually applicable to central scattering may be used. We found that the integral variational expression was sufficiently accurate when the proper component of the plane wave was used as a trial function.

From the relatively small differences shown in Figs. 26 and 27, we decided it was unnecessary to carry out the exact calculations for the nuclear part of the scattering. This is

particularly so because we are able to offset any difference in absolute magnitude by choosing a slightly altered tensor depth (which will be determined only very roughly anyway from the present data). One difficulty with use of the Born approximation is that the interference term (see Appendix 2, for a derivation of this term) between the nuclear and Coulomb scattering identically vanishes, while the exact calculations at 32 Mev show that the P wave component of the nuclear scattering interferes appreciably with the Coulomb scattering. We had therefore to compute two uncoupled phase shifts, δ_1^{00} and $\delta_1^{1\pm}$, and also iterate the coupled $^3P_2 + {}^3F_2$ state. The iteration process is rather tedious and as the magnitudes of the phase shifts, we used the WKB approximation to obtain these phase shifts. We shall consider this approximation in more detail below: If the two independent solutions of the coupled equations have the asymptotic form

$$a_{\ell L} \sim a_{\ell L} \sin(kx - \ell\pi/2 + \delta_{\ell L}^{J}),$$

where $L = \ell$ or $2J - 1$ depending upon which is the dominant state, then the nuclear phase shift may be easily shown to be given by

$$e^{2i\delta_\ell^{Jm_s}} = \frac{e^{i(\delta_{\ell\ell}^J - \delta_{LL}^J)} - a_{\ell L}^J a_{L\ell}^J e^{i(\delta_{\ell L}^J - \delta_{L\ell}^J)} + 2i\left\{\frac{(2L+1)}{(2\ell+1)}\right\}^{\frac{1}{2}} \frac{\langle SLJm_s | SLOm_s\rangle}{\langle S\ell Jm_s | S\ell Om_s\rangle} a_{\ell L}^J \sin(\delta_{\ell\ell}^J - \delta_{\ell L}^J)}{e^{-i(\delta_{\ell\ell}^J + \delta_{\ell L}^J)} - a_{\ell L}^J a_{L\ell}^J e^{-i(\delta_{\ell L}^J + \delta_{L\ell}^J)}}$$

where now $L = 2J - 1$ only, and we have set $a_{\ell\ell}^J = a_{LL}^J = 1$. In the case of the $^3P_2 + {}^3F_2$ state we have found that the Born approximation yields

all quantities in this expression with the exception of δ^2_{11}, with sufficient accuracy. This we have computed by using the "equivalent central potential" in WKB approximation and then applying the Born approximation to this potential to obtain the phase shift. δ^2_{11} is then the sum of two terms one of which is identical with that predicted by the Born approximation applied directly to the coupled equations and the other is of the nature of a correction term, and has the value

$$\Delta^2_{11} = (0.864)/kr \int_0^\infty [xV_t(x)]^2 \, g_1^{\,2} \, (kRx) \, dx,$$

where we have written the tensor potential,

$$S_{12}V_t(r/R) = \left[3(\sigma_1 \cdot r)(\sigma_2 \cdot r)/r^2 - \sigma_1 \cdot \sigma_2\right] V_t(x)$$

and

$$g_\ell (kx) = (\pi kx/2)^{\frac{1}{2}} J_{\ell+\frac{1}{2}} (kx).$$

This procedure applied to the exponential and Yukawa radial dependences yields the coefficients of the interference terms within a few percent the coefficients determined from an exact calculation.

For the 340-Mev scattering the Coulomb scattering was neglected and the singlet scattering was computed in Born approximation.

B. Results

The singlet cross sections for the square, exponential, and Yukawa models are shown in Fig. 28. In each case the range and depth have been chosen to agree with Blatt and Jackson's low energy

analysis. (The range and depth of the Yukawa potential and square well were determined independently by Chew and Goldberger before the results of Blatt and Jackson were available to us and agree within their assigned limits of error.) These parameters, together with the S and D phase shifts at 20 and 32 Mev, are collected in Table I. Clearly there are significant differences in the angular distributions predicted by the various models. However, the magnitude of the D phase shift is always large enough to yield a curve that has a characteristically different shape than the experimental results in the region from 50° to 90° and too low in absolute value at 90°. The principal reason for this is the presence of a P_2 coefficient in the nuclear scattering arising from the interference between the S and the D waves.

The addition of a central P wave does not change the cross section at 90° as can be seen in Fig. 29 where we have indicated the effect of adding positive and negative P phase shifts to the scattering predicted by the Yukawa model (which comes closest to fitting the 90° point). Clearly these curves do not agree with the experimental results, primarily because the nuclear cross section adds in the region from 50° to 90° (where the Coulomb interference can be neglected).

It is seen from Table VI that the D phase shift increases as the potential becomes more long-tailed. Since the D phase shift is too large even for the square potential we are forced to turn to more complicated radial forms if we wish to account for the 32-Mev scattering by central interactions alone. Such a potential might be expected to be repulsive at long distances and attractive at

short distances. Accordingly some attempts were made to annul the D wave by adding a repulsive lip to the square well. They met with little success, and having regard to the inherent difficulties implicit in such an approach when applied to attempt an explanation of the 340-Mev results, this approach was abandoned.

As discussed in Part II, the effect of adding tensor force in the purely nuclear scattering is to produce a more nearly spherically symmetric angular distribution. The depth of the tensor potential and hence the amplitude of the scattering may be considered arbitrary, and must eventually be chosen to give agreement with the experimental data. In Fig. 30 we have shown the result of adding the tensor scattering to the singlet state scattering. Clearly, if the same radial dependence is assumed to hold for both singlet and triplet states, approximate agreement may be obtained for the exponential potential with depth $V_t = \pm 50$ Mev. If we drop the restriction that the singlet and triplet potentials have the same radial dependence, it is clear that we can obtain better agreement, especially with the photographic data, by using the combination of square well for the singlet potential and Yukawa for the triplet (see Fig. 31, curve I). (This combination utilizes a square well with the constants previously found for the singlet state and a tensor Yukawa well of range 1.25×10^{-13} cm and $V_t = \pm 22$ Mev.)

This model gives an angular distribution essentially similar to S wave scattering at energies below 32 Mev. This is illustrated in Fig. 31 where the distribution due to this model at 32 and 20 Mev is compared to S wave scattering. Clearly a

precise measurement would be needed even at 20 Mev in order to distinguish between this distribution and S wave scattering, although it could be distinguished from singlet scattering that included the D wave. Further, it has been found that the cross section at 90° for this model differs by at most three percent from that due to the partial S wave from a Yukawa potential below 32 Mev. Below 20 Mev the Yukawa singlet scattering at 90° (including the D wave) differs by at most $1\frac{1}{2}$ percent from the cross section predicted by this model.

As was remarked in Part II tensor scattering at 32 Mev is only able to explore the tail of the potential, and consequently there is little uniqueness to the radial form which can be established from the 32-Mev data. To illustrate this we may consider the Born approximation. In this approximation the triplet differential cross section (considering only the nuclear part) is proportional to

$$\sigma(\theta) \sim \left[C^2(\theta) + C^2(\pi - \theta) + C(\theta)C(\pi - \theta)\right] ,$$

where

$$C(\theta) = \frac{M}{\hbar^2 K} \int_0^{\infty} V_t(r/R) g_2(Kr)\, r\,dr, \quad K = 2k \sin \theta/2 .$$

Plots proportional to $C(\theta)$ are shown in Fig. 32 as a function of $\mathcal{L}\left[2kR \sin (\theta/2)\right]$ where $\mathcal{L}$ has been adjusted such that each model predicts almost the same scattering at 32 Mev. (Recall that the Yukawa potential with $R = 1.25 \times 10^{-13}$ cm gave a good fit to the data when combined with a shallow singlet potential.) From these plots we find that the following ranges are practically equivalent with respect to the 32 Mev scattering: $R = 3.8 \times 10^{-13}$cm

(square), $R = 1.0 \times 10^{-13}$ cm (exponential), $R = 1.25 \times 10^{-13}$ cm (Yukawa), $R = 2.0 \times 10^{-13}$ cm^2 $(\exp(-r/R)/(r/R)^2)$.

In the plots of $C(\theta)$ we have chosen the scale of the abscissa such that $C(2kR \sin \theta/2) = 1$ for $\theta = 90^\circ$ with a k corresponding to 32 Mev. For other angles we move up and down the abscissa according to $\sin \theta/2$ (e.g., to obtain the value for $C(180^\circ)$ at 32 Mev read the ordinate for an abscissa $2^{\frac{1}{2}}$). The 90° point at other energies can be readily located as it is given at an abscissa which is the square root of the ratio of that energy to 32 Mev. Thus to obtain the value of $C(90^\circ)$ at 350 Mev read the ordinate at an abscissa of $(350/32)^{\frac{1}{2}} = 3.30$.

As the energy increases a large difference in the scattering occurs between the various models. We shall first adjust the range and depth of the tensor potential to fit the data at 32 Mev, then examine the predictions of the various models at 340 Mev. From the predictions of the singlet cross section at 90° it seems reasonable to allow approximately one-third of the nuclear scattering at 32 Mev to be of tensor origin. This fixes the depths of the tensor potentials for a given range. The requirement that the tensor scattering at 32 Mev have sufficient angular variation to mask the singlet D wave sets limits on the range of the potentials.

The 340-Mev cross section is comparable with the fraction of the 32-Mev cross section attributed to tensor scattering. The square, exponential and Yukawa potentials all give too little scattering at 340 Mev (especially around 90°). Shorter ranges for these forms would give better agreement, but these ranges are

incompatible with the 32-Mev data. Comparison between the radial forms indicates that a potential more singular than the Yukawa might give agreement. It was found that a tensor potential of the form $\exp(-r/R)/(r/R)^2$ with $R \cong 1.6 \times 10^{-13}$ cm and $V_t \cong \pm 18$ Mev gives a good fit to both the 32- and the 340-Mev data (see Figs. 31 and 33).

In order to indicate the essential features of the singular model, we again examine the curves in Fig. 32. Clearly a square well of range 4×10^{-13} cm gives scattering of the correct form to fit the 32 Mev data, while a square well of range 1×10^{-13} cm gives 340-Mev scattering approximating to that predicted by the singular model. By combining the shallow long range square well with a deep short range square well (which will not be explored by 32 Mev P wave protons) scattering approximating to that predicted by the singular model can be obtained. Thus a strong tensor interaction at distances less than 1×10^{-13} cm is indicated by the 340-Mev data, while the 32-Mev data gives evidence of interaction at greater distances (i.e., of a "tail" in the terminology of potential models).

SECTION III - SUMMARY AND CONCLUSION

I. Summary of N-P Results

A. Exchange Character

If the potential has approximately the same radial dependence in all states (i.e., even and odd parity, singlet and triplet, central and tensor) and the range is chosen within limits set by the low and high energy scattering, we conclude that for a good fit, we must have $a = 0.55 \pm 0.05$ in the space exchange operator $(1 - a + aP_x)$. More generally, allowing for a different exchange character in singlet and triplet states, the depths of the odd parity potential, V_{odd}, must satisfy the approximate relation

$$0 > \frac{1}{4}({}^1V_{odd}) + \frac{3}{4}({}^3V_{odd}) > -\frac{1}{5}({}^3V_{even}) \quad .$$

In the case when the only odd force is a tensor force the effect on the angular distribution is not as pronounced as in the central force case, because of a partial cancelation of s-p interference terms. The limitation on the strength arises now from a rapid increase in total cross section (for numerical results see Table III).

B. Radial Dependence

The $(\frac{1}{2} + \frac{1}{2}P_x)$ potentials, when compared for equal effective ranges differ by at most a factor of two in the total cross sections or in the ratio $\sigma(180^\circ)/\sigma(90^\circ)$ at 40 Mev and 90 Mev. These differences may be correlated with general shape features and even these two energies are quite adequate to distinguish among the potential shapes. We find that:

1. A long-tailed potential is necessary to explain the large scattering from the higher angular momentum states at 40 Mev without violently affecting the 90-Mev scattering. On this basis the square and Gauss potentials are unacceptable while the exponential and Yukawa wells are allowable. The Yukawa potential is the only potential that has a sufficiently long tail to also be compatible with the 27.2 Mev and 280 Mev angular distributions.

2. The Yukawa potential predicts total cross sections that agree with the experimental results at energies below 30 Mev and at 280 Mev but are 20 to 30 percent too high in the 40 to 90 Mev range. This is because of the singular nature of the Yukawa potential which is required at low energies to balance the tail and give the correct effective range. The exponential which as a smaller tail and is consequently less singular predicts cross sections 10 to 20 percent lower. The best fit for these potentials (assuming the same radial dependence in singlet and triplet state and for central and tensor force) is

$$R = 1.35 \times 10^{-13} \text{ cm.}$$
$$^3V_c = 25.3 \text{ Mev}$$
$$^3V_t = 48.2 \text{ Mev} \qquad \text{(Yukawa)}$$
$$^1V_c = 39.27 \text{ Mev,}$$

and

$$R = 0.75 \times 10^{-13} \text{ cm.}$$
$$^3V_c = 69 \text{ Mev}$$
$$^3V_t = 128 \text{ Mev} \qquad \text{(exponential)}$$
$$^1V_c = 98.6 \text{ Mev.}$$

(For calculations involving the n-p interaction in which it is desired to neglect the tensor interaction a Yukawa range of 1.18×10^{-13} cm with ${}^3V_c = 67.9$ Mev and ${}^1V_c = 46.7$ Mev, may be used.)

3. The shape of the angular distribution about 90° is evidence of a tensor force (in the even triplet states) in scattering. Here, with a $(\frac{1}{2} + \frac{1}{2}P_x)$ dependence, a purely central force yields a flatter distribution than an interaction including tensor force. The latter distribution agrees significantly better with experiment.

C. Singlet Range

The low energy scattering and photo-disintegration phenomena indicate a singlet effective range between 2×10^{-13} and 3×10^{-13} cm. The total cross sections at 40 and 90 Mev as well as the angular distribution imply a singlet range greater than 2×10^{-13} cm.

D. Triplet Range

The triplet effective range in the shape independent approximation is determined from the binding energy and the zero energy scattering to be 1.68×10^{-13} cm. With the long tail that is necessary to fit the high energy scattering the shape independent approximation is not valid and we must fit directly the binding energy and triplet scattering length. This yields somewhat lower values for the effective range (see Table IV). The determination of the range from the high energy scattering depends upon the explicit model used and is compatible with the low energy limits only in the case of the long tailed potentials.

E. Tensor Force Range

The tensor force range may be increased relative to the central range by asmuch as a factor of two without adversely affecting either the low or high energy results.

II. Summary of P-P Results

The 32-Mev data can be fitted by two combinations of central and tensor force. Both have the radial dependence singular for the tensor potential and shallow and cut off for the central potential. The best fit is with a square well of range 2.6×10^{-13} cm and $V_t \exp(-r/R)/(r/R)$ radial dependence (with $R = 1.25 \times 10^{-13}$ cm and $V_t = \pm 23$ Mev) or with a more singular potential $V_t \exp(-r/R)/(r/R)^2$ (with $R = 1.6 \times 10^{-13}$ cm and $V_t = \pm 18$ Mev). These combinations give better fits to the photographic data than to the counter data.

To fit the 340-Mev data we have shown that a very singular tensor force must be used, such as $V_t \exp(-r/R)/(r/R)^2$. The essential feature is that there must be a strong interaction in regions less than 0.5×10^{-13} cm.

The best fit of the combined data is therefore obtained by using the singular potential so adjusted that approximately one-third of the nuclear scattering at 32 Mev is accountable to tensor scattering.

The present data is not sufficiently extensive to permit exploration of more than the salient features of each model. The radial forms are, of course, only partially specified.

III. Conclusions

We have shown that it is possible to fit with a fair approximation all the present n-p and p-p data by means of a charge dependent potential model with monotonous radial dependences.

Quite apart from the potential model assumed, a casual comparison of the p-p data at 32 Mev with the n-p data at 40 Mev and, especially a comparison of the 340 Mev p-p data with the 280 Mev n-p data seems to indicate that the nuclear scattering is charge dependent. This comparison however does not furnish a proof, for it is possible that the difference in the n-p and p-p behavior could be accounted for by the various n-p states that do not occur in p-p system because of the exclusion principle. Therefore in order to examine the possibility for charge independence we must compare the explicit models.

The most outstanding difference between the two models is that the p-p requires an odd tensor interaction to explain the 340 Mev scattering while the n-p system shows none or only a weak interaction in the odd parity states. To put this on a quantitative basis we note from Fig. 23 that the tensor scattering adds about 4 mb/steradian to the p-p cross section at energies between 32 and 340 Mev so that the same forces present in odd triplet n-p states would increase the total n-p cross section by nearly $1/4(4\pi)(4\text{ mb})$ or 12 mb. However the measured n-p cross section at 90 Mev is 75 mb with less than 10 percent uncertainty while the lowest value predicted by a tensor model with only even parity states is 87 mb, so that an additional 12 mb is hard to tolerate. A similar situation

exists at 40 and 90 Mev. Alternatively, a Yukawa tensor potential of range 1.35×10^{-13} cm must be 17.4 Mev deep to fit the 32 Mev data, while the maximum allowable depth of the n-p tensor potential for the same states is 9 Mev (see Table III and Fig. 12).

In order to have charge independence one of the first requirements is to find an n-p model which decreases the even parity total cross section. This requirement may be shown in the case of central forces to be incompatible with the requirement that the potential have a long-tail in order to explain the energy variation of the angular distribution. To show this we recall that the effective range is determined from the formula,

$$r = 2\int_0^\infty \left[\left(\frac{x}{a} + 1\right)^2 - u^2(x)\right] dx \quad ,$$

where a is the scattering length and $u(x)$ is the zero energy solution normalized so that for large x, $u(x)$ behaves like $\left(\frac{x}{a} + 1\right)$. The integrand then differs from zero only inside the range of nuclear forces and is positive everywhere since the range of nuclear forces is smaller than the scattering length and the potential is attractive. It is therefore clear that if the potential has a long-tail, then it must also have a strong attractive region at short distances in order to give a sufficiently short effective range. This strong attractive region however leads to large s-wave cross sections at high energies. It follows from the above effective range argument that if a repulsive core is added even less of a tail can be tolerated so that a fit of the n-p data can not be attained by this means.

The addition of tensor forces having the same radial dependence as the central force was shown in Section I to increase the total cross section. We must, consequently, examine the possibility of using different radial dependences for the central and tensor forces. Consider explicitly the case where the central force has a repulsive core combined with a tensor force having a long tail. The quadrupole moment can then be achieved by a relatively weak tensor force. There will then be only a small modification of the scattering behavior of the $^3S_1 + {}^3D_1$ state (i.e., the state that is predominently an S-state) compared with that of the central force. The higher states particularly the D-states, will however be affected more strongly by the tensor force because of its long range and may be able to account for experimental angular distributions. Detailed calculations with such a model are needed to ascertain to what extent the n-p total cross section may be lowered and still retain the correct angular distribution.

Additional evidence for such a model may be cited: (1) The calculation of the binding energy of the three particle systems using the known n-p and p-p interaction with tensor forces and postulating charge independence and the absence of many body forces lead to binding energies that are too small. The correct binding energy is attained however when a purely central force is assumed for the n-p and p-p interaction leading one to believe that the tensor force does not bind as effectively in three particle systems. A long range tensor force accounts for little of the

binding in the n-p system and hence leads to better values for the binding energy in the three particle system[18]. (2) A model using the combination of a repulsive core for the central p-p interaction and a long tailed tensor force has been found by Jastrow[19] to fit the p-p data. He has also given an explanation of the energy variation of the cross sections for scattering of neutrons on heavier nuclei using the repulsive core central interaction[20].

A more direct knowledge of the charge independence of nuclear forces would be possible if the n-n interaction were known. There are several experimental results which support the hypothesis of charge independence. These are: (1) the binding energy of mirror nuclei differs only by an amount attributable to Coulomb forces; (2) the excess of the number of neutrons over the number of protons in heavy nuclei is again accountable by Coulomb forces; and (3) the large degree of similarity in n-d and p-d scattering at 3 Mev[21] and

---

18 R. Pease and H. Feshbach, Phys. Rev. 78, 322 (1950); E. Gerjuoy and J. Schwinger, Phys. Rev. 61, 138 (1942).

19 R. Jastrow, Phys. Rev. 79, 389 (1950).

20 R. Jastrow, Bull. Am. Phys. Soc. 25, No. 5, 37 (1950).

21 Compare experimental results by S. L. Martin, E. H. S. Burhop, C. B. Alcock and R. L. F. Boyd, Proc. Phys. Soc. 63, 884 (1950); Hamouda, J. Halter and P. Scherrer, Phys. Rev. 79, 539 (1950); J. F. Darby and J. B. Swan, Aust. J. Sci. Res. A. 1, 18 (1948); J. H. Coon and H. H. Barschall, Phys. Rev. 70, 592 (1946); all of whom used incident neutrons energies of approximately 3 Mev with the experimental results of R. Sherr, J. M. Blair, H. R. Kratz, C. L. Bailey and R. F. Taschek, Phys. Rev. 72, 662 (1947); for p-d scattering with incident protons of 1.51 to 3.53 Mev.

at 5 Mev[22], in the angular region where interference with Coulomb scattering is negligible. Unfortunately the direct comparison of the n-d and p-d scattering data over this range cannot be completely justified for the addition of Coulomb forces also affects the nuclear phase shifts[23] (by amounts up to 20%). Theoretical work on the n-d and p-d scattering both at low and high energies assuming the known n-p and p-p interactions should yield considerable information on the n-n interaction. The analysis would be considerably simplified if the n-p and p-p interaction were central or predominantly central. This would be the case at low energies if the long range tensor force model could be used.

We have thus found that potential models can be found which independently explain the n-p and p-p scattering but when taken together they form a complicated model of nuclear forces. Additional theoretical work is necessary to determine if the n-p and p-p scattering can be accounted for by a simplified charge independent nuclear model.

---

22 Compare experimental results by F. A. Rodgers, H. A. Leiter and P. G. Kruger, Phys. Rev. 78, 656 (1950); J. C. Allred and L. Rosen, Phys. Rev. 79, 727 (1950); K. B. Mather, H. J. Karr and R. O. Bondelid, Phys. Rev. 78, 292 (1950) all of whom used approximately 10 Mev deuterons on protons (equivalent to 5 Mev protons on deuterons) with the experimental results of E. Wautuch, Phys. Rev. 79, 729 (1950) for incident neutron of energy 4.5 and 5.5 Mev on deuterons.

23 J. L. Gammel, Phys. Rev. 78, 321 (1950).

Finally, we must take notice of the fact that no large repulsive forces have shown up in either the n-p or the p-p system of sufficient magnitude to account for nuclear saturation if saturation is to be predicted from two body forces. In both cases they would have been very easily detected in the scattering independent of the potential mode assumed.

APPENDIX I

For a scattering problem involving two particles, the Schroedinger equation is

$$\Delta\psi + \frac{2M'}{\hbar^2}(E' - V)\psi = 0 \ , \qquad (1)$$

where V has the form

$$V = (1 - a + aP_x)\left[A(\frac{r}{r_o}) + \beta\,\vec{\sigma}_1\cdot\vec{\sigma}_2\,B(\frac{r}{r_o}) + \gamma\,S_{12}\,C(\frac{r}{r_o})\right] .$$

M' is the reduced mass and E' the energy in the center of mass system. P_x is the Majorana space exchange operator. S_{12} the tensor operator. A, B and C are radial functions with no singularities except possibly a first order pole at $r = 0$ and vanish faster than $1/r$ as $r \longrightarrow \infty$, so that a parametric range, r_o, may be defined.

Since S_{12} vanishes for the singlet state the analysis is the same as for central forces and we may concern ourselves with only the triplet state. (In which case we may as well take $\beta = 0$, and make a corresponding new defination of A(r).)

The wave function of a triplet state of given J, m and parity satisfying the boundary condition at the origin may be written as

$$\psi_\alpha^{Jm}(r, \theta, \phi, m_s) = \frac{1}{r}\sum_l U_{l\alpha}^J(r)\, f_{Jm}^l(\theta, \phi, m_s) \ . \qquad (2)$$

The index α is as yet undefined and expresses the fact that the boundary condition at the origin ($U_{l,\alpha}^J(0) = 0$) does not completely determine the wave function. We anticipate that the ψ^{Jm} representing a physical state will be particular linear combination

of the ψ_α^{Jm} defined by (2).

The f_{Jm}^{ℓ} are compounded from the triplet spin functions and the angular functions (spherical harmonics) by recognizing that the individual functions each are a basis for representation of the rotation group, and reducing the product functions. That is, representations of the rotation operator P_R in the angular-function and triplet spin function space are

$$P_R Y_\mu^\ell (\theta, \phi) = \sum_{\mu'} D^\ell_{\mu\mu'} (R)\, Y^\ell_{\mu'} (\theta, \phi) \qquad \text{and}$$

$$P_R \chi'_\mu (m_s) = \sum_{\mu'} D'_{\mu\mu'} (R)\, \chi'_{\mu'} (m_s)$$

respectively. Hence the basis function for representation of the operator P_R in the various $(2\ell+1)$, $(2\ell+3)$ and $(2\ell-1)$ dimensional product spaces is obtained by the unitary transformation

$$f^{\ell}_{Jm}(\theta, \phi, m_s) = \sum_{\mu=m-1}^{\mu=m+1} S^{\ell\prime}_{J,\mu,\, m-\mu}\, Y^{-\ell}_{\mu}(\theta, \phi)\, \chi'^{(m_s)}_{m-\mu} \qquad \text{Wigner notation}$$

$$F^{Jm}_{\ell}(\theta,\phi) = \sum_{\mu=m-1}^{\mu=m+1} \langle S, \ell, m, m-\mu \,|\, S, \ell, J, m\rangle\; Y^{-\ell}_{m}(\theta,\phi)\, \chi'_{m-\mu} \qquad \text{Ashkin-Wu notation (Phys. Rev. 73, 973 (1948)).}$$

The various elements of the matrices $S^{\ell\prime}_J$ are given in the table below.

J \ ν	-1	0	1
$\ell-1$	$\sqrt{\frac{(\ell+\mu)(\ell+\mu-1)}{(2\ell)(2\ell+1)}}$	$-\sqrt{\frac{(\ell-\mu)(\ell+\mu)}{\ell(2\ell+1)}}$	$\sqrt{\frac{(\ell-\mu-1)(\ell-\mu)}{2\ell(2\ell+1)}}$
ℓ	$\sqrt{\frac{(\ell-\mu+1)(\ell+\mu)}{2\ (\ \ 1)}}$	$\frac{\mu}{\sqrt{\ell(\ell+1)}}$	$-\sqrt{\frac{(\ell+\mu+1)(\ell-\mu)}{2\ell\ (\ell+1)}}$
$\ell+1$	$\sqrt{\frac{(\ell-\mu+1)(\ell-\mu+2)}{(2\ell+1)(2\ell+2)}}$	$\sqrt{\frac{(\ell-\mu+1)(\ell+\mu+1)}{(2\ell+1)(\ell+1)}}$	$\sqrt{\frac{(\ell+\mu+1)(\ell+\mu+2)}{(2\ell+1)(2\ell+2)}}$

The representation of the tensor operator S_{12} in the spin-angular space is

$\ell \backslash \ell'$	J-1	J	J+1
J-1	$-\frac{2(J-1)}{2J+1}$	0	$+\frac{3\sqrt{J(J+1)}}{2J+1}$
J	0	+2	0
J+1	$\frac{3\sqrt{J(J+1)}}{2J+1}$	0	$-\frac{2(J+2)}{2J+1}$

The result of substituting (2) in (1) is

$$\left(\frac{d^2}{dx^2} - \frac{\ell(\ell+1)}{x^2} + \kappa^2 - V^J_{\ell,L}(x)\right) U^J_{\ell\alpha}(x) = 0 \qquad (3)$$

where we have introduced thedimensionless quantities, $x = r/r_o$ and $\kappa = \sqrt{\frac{2M'E'}{\hbar^2}}\, r_o$. The only non-vanishing $V^J_{\ell,L}$ are

$$V^J_{J,J}(x) = (1-a+a(-)^J) \cdot \frac{2M'r_o^2}{\hbar^2} \left[A(x) + 2\gamma C(x)\right] \qquad (4a)$$

$$V^J_{J+1,J-1}(x) = (1-a+a(-)^{J-1}) \cdot \frac{2M'r_o^2}{\hbar^2} \left[A(x) - \frac{2(J-1)}{2J+1}\gamma C(x)\right] \qquad (4b)$$

$$V^J_{J+1,J+1}(x) = (1-a+a(-)^{J+1}) \cdot \frac{2M'r_o^2}{\hbar^2} \left[A(x) - \frac{2(J+1)}{2J+1}\gamma C(x)\right] \qquad (4c)$$

$$V^J_{J-1,J+1}(x) = V^J_{J+1,J-1}(x) = (1-a+a(-)^{J+1}) \cdot \frac{2M'r_o^2}{\hbar^2} \left[\frac{6\sqrt{J(J+1)}}{2J+1}\gamma C(x)\right] \qquad (4d)$$

We notice from (3) and (4) that in the case $J = \ell$ we have a second order differential equation and in the cases $J = \ell \pm 1$ we have coupled second order systems. In the first case we may evidently take $\alpha = L = \ell$. In the other cases we get two solutions which are regular at the origin so we specify these as being solutions to the integral equations

$$U^J_{J-1,L}(x) = A^J_{J-1,L}\, g_{J-1}(kx) + \int_0^\infty G_{J-1}(x:x')\left(V^J_{J-1,J-1}(x')\, U^J_{J-1,L}(x') + V^J_{J-1,J+1}(x')\, U^J_{J+1,L}(x')\right) dx'$$

$$U^J_{J+1,L}(x) = A^J_{J+1,L}\, g_{J+1}(kx) + \int_0^\infty G_{J+1}(x:x')\left(V^J_{J-1,J+1}(x')\, U^J_{J-1,L}(x') + V^J_{J+1,J+1}(x')\, U^J_{J+1,L}(x')\right) dx' \qquad (5)$$

where $A^J_{J\pm1,L}$ are arbitrary constants, and where we have let $\alpha = L$ (and has the values $J-1$ or $J+1$), and

$$G_J(x:x') = \frac{1}{k}\left[g_J(kx)_< \; g_{-J}(kx)_>\right]$$

where $x_<$ means the lesser of x and x' and $g_J(kx)$ and $g_{-J}(kx)$ are the regular and irregular spherical Bessel functions of order $J + \frac{1}{2}$, normalized to sines and cosines at infinity. The asymptotic behavior of (5) is then of the form

$$U^J_{\ell L}(x) \xrightarrow{x} a^J_{\ell L} \sin\left(kx - \frac{\ell\pi}{2} + \delta^J_{\ell L}\right), \qquad (6)$$

where for example,

$$\tan\delta^{J}_{J-1,J-1} = -\left(\frac{1}{A^{J}_{J-1,J-1}}\right)\left(\frac{2M'r_o}{\hbar^2 k}\right)\int_0^{\infty}(V^{J}_{J-1,J-1}(x)\,U^{J}_{J-1,J-1}(x) + V^{J}_{J+1,J-1}(x)\,U^{J}_{J+1,J-1}(x))g_{J-1}(\gamma x)dx,$$

and similar relations for the remaining quantities may easily be found.

The solutions are further subject to the Wronskain condition

$$U^{J}_{J-1,J-1}(U^{J}_{J-1,J+1})' - (U^{J}_{J-1,J-1})'\,U^{J}_{J-1,J+1} + U^{J}_{J+1,J-1}(U^{J}_{J+1,J+1})' - (U^{J}_{J+1,J-1})'\,U^{J}_{J+1,J+1} = 0 \tag{7}$$

which when evaluated for $x \longrightarrow \infty$ yields the relation,

$$a^{J}_{\ell L}\sin(\delta^{J}_{\ell\ell} - \delta^{J}_{\ell L}) = a^{J}_{L\ell}\sin(\delta^{J}_{\ell L} - \delta^{J}_{L\ell}) \tag{8}$$

and we have chosen $a^{J}_{\ell\ell} = a^{J}_{LL} = 1$.

This condition results from the orthogonality of the solutions, for on multiplying the differential equations for $U_{\ell L}$ and $U_{\ell' L}$ by $U_{\ell\ell}$ and $U_{\ell'\ell}$ respectively, integrating and subtracting the same quantities with the indices ℓ and L interchanged we are led to the result

$$U^{J}_{J-1,J-1}(U^{J}_{J-1,J+1})' - (U^{J}_{J-1,J-1})'U^{J}_{J-1,J+1} + U^{J}_{J+1,J-1}(U^{J}_{J+1,J+1})' - (U^{J}_{J+1,J-1})'\,U^{J}_{J+1,J+1} = \text{constant},$$

which when evaluated at the origin gives the constant equal to zero.

We will continue setting up the scattering problem. The wave function ψ_{m_s}, representing a given m_s state in the incident plane wave, can be expanded on the form

$$\psi_{m_s} = \sum_{J,L,m} b_L^{J,m} \psi_L^{J,m} \tag{9}$$

$$= \frac{1}{kr} \sum_{J,\ell,L\,m} b_L^{Jm} U_{\ell L}^{J}(r) f_{Jm}^{\ell} \tag{9'}$$

which is asymptotically

$$\psi_{m_s} \xrightarrow{r} \frac{1}{kr} \sum_{J,\ell,L,m} b_L^{Jm} a_{\ell L}^{J} \sin\left(kr - \frac{\ell\pi}{2} + \delta_{\ell L}^{J}\right) f_{Jm}^{\ell} \tag{10}$$

At great distances from the scattering center ψ_{m_s} can be resolved into the incident plane wave and an outgoing spherical wave originating at the scatterer

$$\psi_{m_s}(r,\theta,\phi) \longrightarrow e^{i\vec{k}\cdot\vec{r}} \chi'_{m_s} + \frac{e^{ikr}}{r} F_{m_s}(\theta,\phi) \tag{10'}$$

where θ and ϕ are the co-latitude and azimuth of the direction of scattering, $\vec{k}'$, with respect to any fixed plane passing through the spin axis. The expansion of a plane wave into normalized spherical harmonics is given by

$$e^{i\vec{k}\cdot\vec{r}} = \frac{1}{kr} \sum_{\ell} (2\ell+1)\, i^{\ell}\, g_{\ell}(kr)\, P_{\ell}(\theta) \tag{11}$$

$$\frac{1}{kr} \sum_{\ell} \sqrt{4\pi(2\ell+1)}\; i^{\ell} g_{\ell}(kr)\; \bar{Y}_o^{\ell}(\theta,\phi) \,. \tag{11'}$$

Expanding in terms of the spin-angular functions the product

$$e^{i\vec{k}\cdot\vec{r}}\chi'_{m_s} = \frac{1}{kr}\sum_{J\ell}\sqrt{4\pi(2\ell+1)}\; i^{\ell}\, g_{\ell}(kr)\, S^{\ell\ell}_{J,0,m_s}\, f^{\ell}_{Jm_s}\ , \qquad (12)$$

this gives asymptotically

$$e^{i\vec{k}\cdot\vec{r}}\chi'_{m_s} \xrightarrow{r} \frac{1}{kr}\sum_{J\ell}\sqrt{4\pi(2\ell+1)}\; i^{\ell}\, S^{\ell\ell}_{J,0,m_s}\sin\left(kr-\frac{\ell\pi}{2}\right) f^{\ell}_{Jm_s}\ . \qquad (12')$$

Writing ψ_{m_s} in the form (10) by adding and subtracting the left and right hand sides of (12') we find

$$\psi_{m_s} \xrightarrow{r} e^{i\vec{k}\cdot\vec{r}}\chi'_{m_s} + \sum_{J\ell m}\left\{\sum_L b^{Jm}_L\, a^{J}_{\ell L}\sin\left(\frac{kr-\frac{\ell\pi}{2}+\delta^J_{\ell L}}{kr}\right)\right.$$

$$\left. -\delta_{mm_s}\sqrt{4\pi(2\ell+1)}\; i^{\ell}\, S^{\ell\ell}_{J,0,m}\sin\frac{\left(kr-\frac{\ell\pi}{2}\right)}{kr}\right\} f^{\ell}_{Jm}\ . \qquad (13)$$

Expanding the term in the curly bracket of (13) we have

$$\{\cdots\} = \frac{e^{ikr}}{2ikr}\left[\sum_L b^{Jm}_L\, a^{J}_{\ell L}\,(i)^{-\ell} e^{i\delta^J_{\ell L}} - \delta_{mm_s}\sqrt{4\pi(2\ell+1)}\; S^{\ell\ell}_{J,0,m}\right]$$

$$-\frac{e^{-ikr}}{2ikr}\left[\sum_L b^{Jm}_L\, a^{J}_{\ell L}\,(i)^{\ell} e^{-i\delta^J_{\ell L}}\right.$$

$$\left. -\delta_{mm_s}\sqrt{4\pi(2\ell+1)}\; S^{\ell\ell}_{J,0,m}(i)^{2\ell}\right].$$

For out-going spherical waves the coefficient of $\frac{e^{-ikr}}{r}$ must vanish

for each ℓ, we have then $m = m_s$ and the following system for the determination of the unknown coefficients b_L^{Jm}

$$\sum b_L^{Jm_s} \; a_{\ell L}^{J} \; e^{-i\delta_{\ell L}^{J}} = \sqrt{4\pi(2\ell+1)} \; S_{J,0,m_s}^{\ell l} \, (i)^{\ell} . \tag{14}$$

The result of solving for $b_\ell^{Jm_s}$ is

$$b_J^{Jm_s} = \sqrt{4\pi(2\ell+1)} \; i^{J} \, e^{i\delta_{JJ}^{J}} \; S_{J,0,m_s}^{Jl} \quad , \text{ when } L = J, \tag{15a}$$

$$b_{J-1}^{Jm_s} = \frac{\sqrt{4\pi}}{D} \; i^{J-1} \left(\sqrt{2J-1} \; S_{J,0,m_s}^{J-1,1} \; e^{-i\delta_{J+1,J+1}^{J}} \right.$$

$$\left. + \sqrt{2J+3} \; S_{J,0,m_s}^{J+1,1} \; a_{J-1,J+1}^{J} \; e^{-i\delta_{J-1,J+1}^{J}} \right) , \tag{15b}$$

when $L = J-1$, and

$$b_{J+1}^{Jm_s} = \frac{\sqrt{4\pi}}{D} \; i^{J+1} \left(\sqrt{2J+3} \; S_{J,0,m_s}^{J+1,1} \; e^{-i\delta_{J-1,J-1}^{J}} \right.$$

$$\left. + \sqrt{2J-1} \; S_{J,0,m_s}^{J-1,1} \; a_{J+1,J-1}^{J} \; e^{-i\delta_{J+1,J-1}^{J}} \right) , \tag{15c}$$

when $L = J+1$, where D is the determinant,

$$D = \left[e^{-i(\delta_{J-1,J-1}^{J} + \delta_{J+1,J+1}^{J})} \; -a_{J+1,J+1}^{J} \; a_{J-1,J+1}^{J} \; e^{-i(\delta_{J-1,J+1}^{J} + \delta_{J+1,J-1}^{J})} \right] . \tag{16}$$

We can now write (13) in the form

$$\psi_{m_s} \xrightarrow{r} e^{i\vec{k}\vec{r}}\chi'_{m_s} + \frac{e^{ikr}}{r} \sum_{J\ell}\sqrt{\frac{4\pi(2\ell+1)}{2ik}}\,(e^{2i\delta_\ell^{Jm_s}} - 1)\, S^{\ell 1}_{J,0,m_s}\, f^{\ell}_{Jm_s}\,, \tag{17}$$

where we have introduced the abbreviations,

$$e^{2i\,\delta_J^{Jm_s}} = e^{2i\,\delta_{J,J}^{J}}\,, \text{ and} \tag{18a}$$

$$e^{2i\,\delta_{J\pm1}^{Jm_s}} = \frac{e^{i(\delta_{\ell\ell}^{J} - \delta_{LL}^{J})} - a^{J}_{\ell L}\, a^{J}_{L\ell}\, e^{i(\delta_{\ell L}^{J} - \delta_{L\ell}^{J})} + 2i\left(\frac{S^{L1}_{JOm_s}\sqrt{2L+1}}{S^{\ell 1}_{JOm_s}\sqrt{2\ell+1}}\right) a^{J}_{\ell L}\sin(\delta_{\ell\ell}^{J} - \delta_{\ell L}^{J})}{e^{-i(\delta_{\ell\ell}^{J} + \delta_{LL}^{J})} - a^{J}_{\ell L}\, a^{J}_{L\ell}\, e^{-i(\delta_{\ell L}^{J} + \delta_{L\ell}^{J})}} \tag{18b}$$

In calculations it is convenient to note

$$\sqrt{\frac{2(J+1)+1}{2(J-1)+1}}\;\frac{S^{J+1,1}_{JO\pm}}{S^{J-1,1}_{JO\pm}} = \sqrt{\frac{J}{J+1}} \quad \text{and} \quad \sqrt{\frac{2(J-1)+1}{2(J+1)+1}}\;\frac{S^{J-1,1}_{JOO}}{S^{J+1,1}_{JOO}} = -\sqrt{\frac{J}{J+1}}$$

If we write (17) in the forms

$$\psi_{m_s} \xrightarrow{r} e^{i\vec{k}\cdot\vec{r}}\chi'_{m_s} + \frac{e^{ikr}}{r} F_{m_s} \tag{10'}$$

$$= e^{i\vec{k}\cdot\vec{r}}\chi'_{m_s} + \frac{e^{ikr}}{r} \sum_{\mu} \mathcal{S}_{m_s-\mu,m_s}\,\chi'_{m_s-\mu} \tag{19}$$

the matrix elements $\mathcal{S}_{m_s' m_s}$ are identical with those defined by Ashkin and Wu and have the explicit form,

$$\mathcal{S}_{m_s-\mu,m_s} = \frac{1}{2ik} \sum_{J\ell} \sqrt{4\pi(2\ell+1)}\; S^{\ell 1}_{JOm_s}\; S^{\ell 1}_{J,\mu,m_s-\mu}\,(e^{2i\delta_{\ell-1}^{Jm_s}})\; \bar{Y}^{\ell}_{\mu}(\theta,\phi)\,. \tag{20}$$

The differential cross section is found by averaging the square modulus of F_{m_s} over the m_s of the initial wave, giving the result,

$$\frac{d\sigma}{d\Omega} = \frac{1}{3}\sum_{m_s}\left|F_{m_s}\right|^2$$

$$= \frac{4\pi}{3k^2}\sum_{JJ'll'm_s\mu}\sqrt{(2l+1)(2l'+1)}\;S^{l1}_{J0m_s}S^{l1}_{J\mu m_s,-\mu}S^{l'1}_{J'0m_s}S^{l'1}_{J'\mu m_s-\mu}$$

$$\cdot\left(\overline{Y}^{l}_{\mu}(\theta,\phi)\;\overline{Y}^{l*}_{\mu}(\theta,\phi)\,\varepsilon^{JJ'm_s}_{ll'}\right), \tag{21}$$

where

$$\varepsilon^{JJ'm_s}_{ll'} = \frac{1}{4}\left(e^{2i\delta^{Jm_s}_{l}}-1\right)^{*}\left(e^{2i\delta^{J'm_s}_{l'}}-1\right). \tag{22}$$

Writing Eq. (21) explicitly in terms of the Legendre polynomials we have, (23)

$$\frac{d\sigma}{d\Omega} = \frac{\mathrm{Re}}{3k^2}\Bigg\{P_0(\theta)\Big[\varepsilon^{110}_{00}+2\varepsilon^{11\pm}_{00}+\varepsilon^{000}_{11}+3\varepsilon^{11\pm}_{11}+2\varepsilon^{220}_{11}+3\varepsilon^{22\pm}_{11}+2\varepsilon^{110}_{22}$$
$$+\varepsilon^{11\pm}_{22}+5\varepsilon^{22\pm}_{22}+3\varepsilon^{330}_{22}+4\varepsilon^{33\pm}_{22}+\cdots\Big]+P_1(\theta)\Big[2\varepsilon^{010}_{10}+6\varepsilon^{11\pm}_{01}$$
$$+6\varepsilon^{12\pm}_{01}+4\varepsilon^{120}_{01}+4\varepsilon^{010}_{12}+3\varepsilon^{11\pm}_{12}+9\varepsilon^{12\pm}_{12}-\frac{3}{5}\varepsilon^{12\pm}_{21}+\frac{4}{5}\varepsilon^{120}_{21}$$
$$+3\varepsilon^{22\pm}_{12}+\frac{48}{5}\varepsilon^{23\pm}_{12}+\frac{36}{5}\varepsilon^{230}_{12}+\cdots\Big]+P_2(\theta)\Big[4\varepsilon^{110}_{02}+2\varepsilon^{11\pm}_{02}+10\varepsilon^{12\pm}_{02}$$
$$+6\varepsilon^{130}_{02}+8\varepsilon^{13\pm}_{02}+4\varepsilon^{020}_{11}+\frac{3}{2}\varepsilon^{11\pm}_{11}+9\varepsilon^{12\pm}_{11}+\frac{3}{2}\varepsilon^{22\pm}_{11}+2\varepsilon^{220}_{11}+2\varepsilon^{110}_{22}-\frac{1}{2}\varepsilon^{11\pm}_{22}$$
$$+\frac{25}{14}\varepsilon^{22\pm}_{22}+\frac{24}{7}\varepsilon^{33\pm}_{22}+\frac{24}{7}\varepsilon^{330}_{22}+5\varepsilon^{12\pm}_{22}+\frac{40}{7}\varepsilon^{23\pm}_{22}-\frac{8}{7}\varepsilon^{13\pm}_{22}+\frac{12}{7}\varepsilon^{130}_{22}+\cdots\Big]$$
$$+P_3(\theta)\Big[6\varepsilon^{12\pm}_{12}+\frac{18}{5}\varepsilon^{12\pm}_{21}+\frac{36}{5}\varepsilon^{120}_{21}+12\varepsilon^{22\pm}_{12}+6\varepsilon^{030}_{12}+12\varepsilon^{13\pm}_{12}+\frac{12}{5}\varepsilon^{23\pm}_{12}+\frac{24}{5}\varepsilon^{230}_{12}+\cdots\Big]$$
$$+P_4(\theta)\Big[\frac{40}{7}\varepsilon^{22\pm}_{22}+\frac{100}{7}\varepsilon^{23\pm}_{22}+\frac{4}{7}\varepsilon^{33\pm}_{22}+\frac{36}{7}\varepsilon^{13\pm}_{22}+\frac{72}{7}\varepsilon^{130}_{22}+\frac{18}{7}\varepsilon^{330}_{22}+\cdots\Big]+\cdots\Bigg\}$$

The total cross section for an unpolarized beam is found by integrating Eq. (21) over solid angle, with the result,

$$\sigma = \frac{4\pi}{3k^2} \sum \left(S^{\ell l}_{J O m_s}\right)^2 (2\ell+1)\, \mathcal{E}^{J J m_s}_{\ell\ell} \tag{24}$$

$$= \frac{4\pi}{3k^2} \left\{ \mathcal{E}^{110}_{00} + 2\mathcal{E}^{11\pm}_{00} + \mathcal{E}^{000}_{11} + 3\mathcal{E}^{11\pm}_{11} + 2\mathcal{E}^{220}_{11} + 3\mathcal{E}^{22\pm}_{11} + 2\mathcal{E}^{110}_{22} \right.$$

$$\left. + \mathcal{E}^{11\pm}_{22} + 5\mathcal{E}^{22\pm}_{22} + 4\mathcal{E}^{33\pm}_{22} + 3\mathcal{E}^{330}_{22} + \cdots \right\} .$$

In actual calculations we use approximate methods for determining the phase shifts that enter into Eq. (22). We have discussed in the text (See Section I, Part 2, Computational Methods.) the solution of Eq. (5) for the lowest states. We wish here to discuss the addition of all the higher states in Born approximation.

The Born approximation can be made directly on the three dimensional integral equation corresponding to the differential Eq. (1) without the necessity for expanding in spherical harmonics. Thus we have

$$^{(B)}F_{m_s} = \frac{1}{4\pi} \sum_{\mu} \chi'_{m_s-\mu} \int e^{-i\vec{k}\cdot\vec{r}}\, \chi'_{m_s-\mu} \left(\frac{2M'}{\hbar^2} V\right) e^{i\vec{k}\cdot\vec{r}}\, \chi'_{m_s}\, d\vec{r} \tag{25}$$

$$= \frac{1}{4\pi} \sum_{\mu} \chi'_{m_s-\mu} \int e^{-i\vec{k}\cdot\vec{r}} \left[\frac{2m'}{\hbar^2} V_{m_s-\mu, m_s}(\vec{r}) \cdot (1-a+aP_x)\right] e^{i\vec{k}\cdot\vec{r}}\, d\vec{r}, \tag{25'}$$

where

$$V_{m_s-\mu, m_s}(\vec{r}) = \left[A\left(\frac{r}{r_o}\right) - 2^{3/2}\gamma\, S^{21}_{1,\mu,m_s-\mu}\, \bar{Y}^{-2}_{\mu}(\alpha,\beta)\, C\left(\frac{r}{r_o}\right) \right]$$

and the co-latitude and azimuth of $\vec{r}$ with respect to the spin axis is denoted by α and β. Performing the integrations indicated in Eq. (25) we have

$$
{}^{(\beta)}F_{m_s} = \sum_{\mu} \chi'_{m_s-\mu} \Big\{ (1-a)\, F(K) + a F(L) \qquad (26)
$$

$$
- 2^{3/2} \gamma\, S^{21}_{1,\mu,m_s-\mu} \Big[(1-a)\, \bar{Y}^2\left(\frac{\pi}{2} - \frac{\theta}{2}, 0\right) C(K)
$$

$$
+ a \bar{Y}^2\left(\frac{\theta}{2}, \pi\right) C(L) \Big] \Big\} \ ,
$$

where

$$
F(K) = \frac{2M'}{\hbar^2 K} \int_0^{\infty} \sin kr\, A\left(\frac{r}{r_o}\right) r\, dr \ ,
$$

$$
C(K) = \frac{2M'}{\hbar^2 K} \int_0^{\infty} g_2\,(kr)\, C\left(\frac{r}{r_o}\right) r\, dr \ ,
$$

$$
K = 2k \sin \theta/2 \ ,
$$

$$
L = 2k \cos \theta/2 \ .
$$

Explicitly for the Yukawa potential; $A\left(\frac{r}{r_o}\right) = C\left(\frac{r}{r_o}\right) = V_o\left(e^{-r/r_o}/(r/r_o)\right)$, we have

$$
F(K) = \frac{b r_o}{1 + (Kr_o)^2} \ ,
$$

$$
C(K) = \frac{b r_o}{(Kr_o)^2} \left(3 - \frac{(Kr_o)^2}{1+(Kr_o)^2} - \frac{3}{Kr_o} \tan^{-1}(Kr_o)\right)
$$

$$
= b r_o \left(\frac{2}{5}(Kr_o)^2 - \frac{4}{7}(Kr_o)^4 + \frac{6}{a}(Kr_o)^6 - \ldots\right).
$$

where $b = \dfrac{2M' r_o^2}{\hbar^2} V_o$.

Explicitly for the exponential potential, $A(r/r_o) = C(r/r_o) = V_o\, e^{-(r/r_o)}$, we have

$$F(K) = \frac{2br_o}{(1+(Kr_o)^2)^2} ,$$

$$C(K) = \frac{br_o}{(Kr_o)^2}\left(\frac{3}{Kr_o}\tan^{-1}(Kr_o) - \frac{2(Kr_o)^2}{(1+(Kr_o)^2)^2} - \frac{3}{1+(Kr_o)^2}\right)$$

$$= br_o\left(\frac{8}{5}(Kr_o)^2 - \frac{24}{7}(Kr_o)^4 + \frac{48}{9}(Kr_o)^6 - \frac{80}{11}(Kr_o)^8 + \cdots\right)$$

where $b = \frac{2M'r_o^2}{\hbar^2} V_o$.

The differential cross section in Born approximation is

$$\left(\frac{d\sigma}{d\Omega}\right)_B = \left[(1-a)\,F(K) + aF(L)\right]^2 + 8\gamma^2\left[(1-a)^2C(K) + a^2C(L) - (1-a)a\,C(K)C(L)\right] \tag{27}$$

To show the relationship with the phase shift analysis we may calculate the RHS of Eq. (12) using Eq. (12) with the result

$$(F_{m_s})_B = \sum \chi_{m_s-\mu}\sqrt{(2\ell+1)(2L+1)}\,\frac{i^{L-\ell}}{k^2}\int_0^\infty \left(f^{L}_{J'm_s}, \frac{2M'}{\hbar^2}\,V\, f^{\ell}_{Jm_s}\right) g_L(kr)g_\ell(kr)dr \tag{28}$$

$$= \frac{1}{k}\sum\sqrt{4\pi(2L+1)}\, S^{L\ell}_{J0m_s} f^{\ell}_{Jm_s}\, \left(\frac{i}{k}\right)^{L-\ell}\int_0^\infty g_L(kr)g_\ell(kr)\, V^{J}_{\ell L}(r)\, dr \tag{29}$$

Comparing Eq. (29) with Eq. (17) we see that if we make the approximation

$$\frac{e^{2i\delta_\ell^{Jm_s}} - 1}{2i} \simeq \delta_\ell^{Jm_s}$$

which is valid for small phase shifts then we may identify the expression for Born phase shifts as

$$ {}^{(B)}\delta_\ell^{J m_s} = \sum \frac{S^{L\ell}_{J0m_s}}{S^{\ell\ell}_{J0m_s}} \frac{\sqrt{2L+1}}{\sqrt{2\ell+1}} \; i^{\ell-L} \; \frac{1}{k} \int_0^\infty g_L(kr) g_\ell(kr) V^J_{\ell L}(r)\, dr \qquad (30) $$

The result given by Eq. (30) is seen to be identical with that resulting from taking only the first term in the perturbation approximation of Eq. (25) (with $A^J_{\ell L} = \delta_{\ell L}$) and consistantly retaining only terms linear in the potential in the evaluation of Eq. (17).

We may clearly write the expression for the differential cross section, Eq. (21);

$$ \frac{d\sigma}{d\Omega} = {}^{(B)}\frac{d\sigma}{d\Omega} + \frac{1}{3}\sum_{m_s} 2\mathrm{Re}\left\{ {}^{(B)}F_{m_s}\left(F_{m_s} - {}^{(B)}F_{m_s}\right)\right\} + \frac{1}{3}\sum_{m_s} \left| F_{m_s} - {}^{(B)}F_{m_s}\right|^2 . \qquad (31) $$

The second term on the RHS of Eq. (31) may be written as

$$ \frac{1}{3}\sum_{m_s} 2\mathrm{Re}\left\{ {}^{(B)}F_{m_s}\left(F_{m_s} - {}^{(B)}F_{m_s}\right)\right\} = \frac{1}{3k}\sum_{J\ell m_s} \Delta_\ell^{J m_s} \left\{ R_\ell^{J m_s}(\theta)\left[(1-a)F(K) + aF(L)\right] - r\left[(1-a)\, Q_\ell^{J m_s}(K)C(K) + aQ_\ell^{J m_s}(L)C(L)\right]\right\} \qquad (32) $$

where

$$ \Delta_\ell^{J m_s} = \frac{1}{2i}\left(e^{2i\delta_\ell^{J m_s}} - e^{-2i\left(\delta_\ell^{J m_s}\right)^*} - 4i\, {}^{B}\delta_\ell^{J m_s}\right), $$

$$ R_\ell^{J m_s}(\theta) = \sqrt{4\pi(2\ell+1)}\, \left(S^{\ell\ell}_{J0m_s}\right)^2 \overline{Y}^{\ell}_{0}(\theta, 0) \quad , $$

$$Q_\ell^{Jm_s}(K) = 2^{3/2}\sum_\mu \left(\sqrt{4\pi}\, \bar{Y}^2_\mu \left(\frac{\pi}{2} - \frac{\theta}{2}, 0\right) S^{2l}_{1,\mu,m_s-\mu}\right)\left(S^{\ell l}_{J,\mu,m_s-\mu} S^{\ell l}_{J0m_s} \sqrt{4\pi(2\ell+1)} \cdot \left(Y(\theta,0)\right)\right) ,$$

$$Q_\ell^{Jm_s}(L) = 2^{3/2}\sum_\mu (-)^\mu \left(\sqrt{4\pi}\, \bar{Y}^2_\mu \left(\frac{\theta}{2}, 0\right) S^{2l}_{1,\mu,m_s-\mu}\right)\left(S^{\ell l}_{J,\mu,m_s-\mu} S^{\ell l}_{J0m_s} \sqrt{4\pi(2\ell+1)}\ \bar{Y}^{\ell}_{\mu}(\theta,0)\right) .$$

Writing Eq. (32) somewhat more explicitly we have

$$\frac{1}{3}\sum_{m_s} 2\mathrm{Re}\left\{ {}^{(B)}F_{m_s}\left(F_{m_s} - {}^{(B)}F_{m_s}\right)\right\} = \tag{33}$$

$$\begin{aligned}
&\frac{1}{3k}\left[(1-a)F(K) + aF(L)\right]\Big\{ (\Delta_0^{10} + 2\Delta_2^{1\pm})P_0(\theta) \\
&\qquad + (\Delta_1^{00} + 3\Delta_1^{1\pm} + 3\Delta_1^{2\pm} + 2\Delta_1^{20})P_1(\theta) \\
&\qquad + (2\Delta_2^{10} + \Delta_2^{1\pm} + 5\Delta_2^{2\pm} + 3\Delta_2^{30} + 4\Delta_2^{3\pm})P_2(\theta) + \ldots\Big\} \\
&+\frac{1}{3k}\left[(1-a)C(K) + aC(L)\right]\Big\{ (-\Delta_0^{10} + \Delta_0^{1\pm} + \tfrac{3}{2}\Delta_2^{1\pm} - \tfrac{5}{2}\Delta_2^{2\pm} + \Delta_2^{3\pm})P_0(\theta) \\
&\qquad + (-\Delta_1^{00} + \tfrac{3}{2}\Delta_1^{1\pm} + \tfrac{3}{2}\Delta_1^{1\pm} + \tfrac{3}{2}\Delta_1^{2\pm} - 2\Delta_1^{20})P_1(\theta) \\
&\qquad + (-2\Delta_2^{10} - \Delta_2^{1\pm} + 5\Delta_2^{2\pm} - 3\Delta_2^{30} + \Delta_2^{3\pm})P_2(\theta) + \ldots\Big\} \\
&+\frac{1}{3k}\left[(1-a)C(K) - aC(L)\right]\Big\{ (3\Delta_1^{00} - \tfrac{9}{2}\Delta_1^{1\pm} + \tfrac{3}{2}\Delta_1^{2\pm})P_0(\theta) \\
&\qquad + (3\Delta_1^{10} - 3\Delta_0^{1\pm} + 6\Delta_2^{10} - \tfrac{3}{2}\Delta_2^{1\pm} - \tfrac{15}{2}\Delta_2^{2\pm} + 3\Delta_2^{3\pm})P_1(\theta) \\
&\qquad + (6\Delta_1^{20}P_2(\theta) + (9\Delta_2^{30} - 9\Delta_2^{3\pm})P_3(\theta) + \ldots\Big\}
\end{aligned}$$

The third term in Eq. (31), namely $\frac{1}{3}\sum_{m_s} |F_{m_s} - {}^{(B)}F_{m_s}|^2$, can be written out exactly the same as Eq. (21) and Eq. (23), replacing $\varepsilon_{ll'}^{JJ'm_s}$ by $\Delta_{ll'}^{JJ'm_s}$ where

$$\Delta_{ll'}^{JJ'm_s} = \frac{1}{4}\left(e^{2i\delta_l^{Jm_s}} - 2i\,{}^{(B)}\delta_l^{Jm_s} - 1\right)^*\left(e^{2i\delta_{l'}^{Jm_s}} - {}^{(B)}\delta_{l'}^{Jm_s} - 1\right).$$

We sum only over those terms in the second and third terms of Eq. (31) for which we have evaluated the exact phase shifts. The resulting angular distribution will then contain the Born approximation shifts for all the remaining partial waves.

APPENDIX II

The triplet cross section is given by

$$d\sigma/d\Omega = 1/3k^2 \sum_{m_s} (|R|^2 + RN_o^* + N_oR^* + \sum_{\mu} N_\mu^* N_\mu) , \qquad (1A)$$

where

$$R = \alpha/2i \left(\frac{\exp[-i\alpha \ln \sin^2(\theta/2)]}{\sin^2(\theta/2)} - \frac{\exp[-i\alpha \ln \cos^2(\theta/2)]}{\cos^2(\theta/2)} \right),$$

$$N_\mu = \sum_{j,\ell} [4\pi(2\ell + 1)]^{1/2} \exp[2i(\sigma_\ell - \sigma_o)] \langle S\ell J m_s | S\ell 0 m_s \rangle$$

$$\times \langle S\ell J m_s - \mu | S\ell_\mu m_s - \mu \rangle [\exp(2i\delta_\ell^{Jms}) - 1] \quad \bar{Y}_\ell^\mu(\theta,\phi) ,$$

$$\alpha = e^2/\hbar v$$

$$\sigma_\ell - \sigma_o = \tan^{-1} (\alpha/\ell) + \tan^{-1} (\alpha/\ell - 1) + \ldots + \tan^{-1} \alpha$$

$\bar{Y}_\ell^\mu(\theta,\phi)$ are the normalized tesseral harmonics and δ_ℓ^{Jms} are the customary (complex) phase shifts that occur in tensor scattering (defined here in the presence of the Coulomb field).

In Eq. (1A) the term involving $|R|^2$ is just the usual triplet Coulomb scattering and the terms $\sum_\mu N_\mu^* N_\mu$ are the usual nuclear scattering. The remaining terms represent the interference between nuclear and Coulomb scattering.

In our calculations of the tensor scattering the Coulomb modification of the nuclear phase shift was neglected as the expected order of magnitude of this modification was very small compared to the P phase shifts. Further the nuclear-Coulomb interference terms were calculated only for the P wave part of the nuclear scattering. These terms can then

be written

$$\frac{9P_1(\cos\theta)}{2k^2}\left[\frac{\sin\alpha_1}{S^2}-\frac{\sin\beta_1}{C^2}\right]$$

$$\times\left(\frac{1}{9}\sin^2\delta_1{}^{0\,0}+\frac{1}{3}\sin^2\delta_1{}^{1\pm}-\frac{1}{6}A_1{}^{2\pm}-\frac{1}{9}A_1{}^{2\,0}\right)$$

$$-\frac{9P_1(\cos\theta)}{2k^2}\left[\frac{\cos\alpha_1}{S^2}-\frac{\cos\beta_1}{C^2}\right]$$

$$\times\left(\frac{1}{9}\sin\delta_1{}^{0\,0}\cos\delta_1{}^{0\,0}+\frac{1}{3}\sin\delta_1{}^{1\pm}\cos\delta_1{}^{1\pm}+\frac{1}{6}B_1{}^{2\pm}+\frac{1}{9}B_1{}^{2\,0}\right), \quad (2A)$$

where

$$\alpha_1 = a\,\ln S^2 + 2(\sigma_1-\sigma_o)$$

$$\beta_1 = a\,\ln C^2 + 2(\sigma_1-\sigma_o)$$

$$S^2 = \sin^2\theta/2$$

$$C^2 = \cos^2\theta/2$$

$$A_\ell{}^{Jms} = \mathrm{Re}\left[\exp(2i\delta_\ell{}^{Jms})-1\right]$$

$$B_\ell{}^{Jms} = \mathrm{Im}\left[\exp(2i\delta_\ell{}^{Jms})\right]$$

Equation (2A) reduces to the expression given by Breit, Kittel, and Thaxton, Phys. Rev. 57, 255 (1940), when the coupling between the $^3P_2$ and $^3F_2$ scattering is neglected.

Table I

Derived Quantities

Quantity	Notation	Magnitude	Source (with error)
singlet scattering length	l_a	$-23.68 \pm 0.08 \times 10^{-13}$ cm	ortho-para scattering[a] ($\pm 0.03 \times 10^{-13}$ cm) crystal-scattering[b] ($\pm 0.05 \times 10^{-13}$ cm) zero-energy cross section[c] ($\pm 0.06 \times 10^{-13}$ cm) liquid mirror reflection[d] ($\pm 0.02 \times 10^{-13}$ cm)
radius of deuteron	r_d	$4.332 \pm 0.025 \times 10^{-13}$ cm	binding energy[e]
triplet scattering length	3_a	$5.38 \pm 0.05 \times 10^{-13}$ cm	liquid mirror reflection ($\pm 0.03 \times 10^{-13}$ cm) ortho-para scattering ($\pm .09 \times 10^{-13}$ cm) crystal scattering ($\pm .15 \times 10^{-13}$ cm) zero energy cross section ($\pm .03 \times 10^{-13}$ cm)
triplet effective range (shape ind. approx.)	3_r	$1.71 \pm 0.10 \times 10^{-13}$ cm	from ^3a ($\pm 0.08 \times 10^{-13}$ cm) from $^r d$ ($\pm 0.03 \times 10^{-13}$ cm)
singlet effective range	1_r	$2.5 \pm 0.5 \times 10^{-13}$ cm	scattering between 0 and 6 Mev photomagnetic disintegration of deuteron[f]
electric quadrupole moment	Q	$2.73 \pm .05 \times 10^{-27}$ cm^2	directly determined[g]
percent D-state	W_D	3.9 percent	magnetic dipole moment, neglecting relativistic effects

(a) Sutton, Hall, Anderson, Bridge, DeWire, Lavatelli, Long, Snyder, and Williams, Phys. Rev. 72, 1147 (1947).
(b) Shull, Wollan, Morton, and Davidson, Phys. Rev. 73, 842 (1948).
(c) W. B. Jones, Jr., Phys. Rev. 74, 364 (1948); Melkonian, Rainwater, and Havens, Phys. Rev. 75, 1295 (1949).
(d) Hughes, Burgy, and Ringo, Phys. Rev. 79, 227 (1950).
(e) R. E. Bell and L. G. Elliott, Phys. Rev. 74, 1552 (1948); W. E. Stephens, Rev. Mod. Phys. 19, 19 (1947); W. E. Stephens, Phys. Rev. 76, 181 (1949); Tollestrup, Jenkins, Fowler, and Lauritsen, Phys. Rev. 75, 1947 (1949).
(f) H. A. Bethe and C. Longmire, Phys. Rev. 77, 647 (1950).
(g) A. Nordsieck, Phys. Rev. 58, 310 (1940).

Table II

High energy total cross sections. The error in the mean energy arises from uncertainties in detector efficiency, neutron beam distribution, and variation of cross section with energy. The "average" $\sin^2 \delta_s$ is determined by subtracting the contributions of the higher partial waves as derived from the angular distribution on the basis of no spin dependence in scattering.

Mean energy Mev	Total cross section with statistical error 10^{-24} cm.	Detection method	Average $\sin^2\delta_s$
41 ± 4	0.174 ± 0.010	Proton recoils	0.67 ± 0.11[a]
40 ± 4	0.202 ± 0.007	$C^{12}(n,2n)C^{11}$	0.76 ± 0.11[b]
83 ± 7	0.083 ± 0.004	$C^{12}(n,2n)C^{11}$	0.66 ± 0.08[c]
90 ± 3	0.079 ± 0.007	Proton recoils	0.68 ± 0.08[a]
95 ± 5	0.073 ± 0.002	Bi fission	0.66 ± 0.06[d]
156 ± 3	0.0462± 0.0012	Proton recoils[e]	
160 ± 15	0.0512± 0.0026	Bi fission[f]	
240 ± 15	0.0410± 0.0041	Bi fission[f]	
270 ± 15	0.038 ± 0.0015	Bi fission[f]	
280 ± 15	0.033 ± 0.0030	Proton recoils[g]	

(a) Hadley, Kelly, Leith, Segrè, Wiegand, and York, Phys. Rev. 75, 351 (1949).

(b) R.H. Hildebrand and C. E. Leith, Phys. Rev. 76, 587 (1949); also private communication.

(c) Cook, McMillan, Peterson, and Sewell, Phys. Rev. 72, 1264 (1947).

(d) J. DeJuren and N. Knable, Phys. Rev. 77, 606 (1950).

(e) Taylor, Pickavance, Cassels, and Randle, to be published as a letter to the Editors of "Nature."

(f) J. DeJuren and B. J. Moyer, Phys. Rev., in press.

(g) Kelly, Leith, Segrè, and Wiegand, Phys. Rev. 79, 96 (1950).

A. Bratenahl
PR 77 597

Model				90 Mev							40 Mev		
Exchange Dependence	Range (10^{-13} cm)	Radial Dependence	γ	σ (10^{-26} cm^2)	a_1	a_2	a_3	a_4	$\frac{\sigma(180)}{\sigma(90)}$	$\frac{\sigma(0)}{\sigma(90)}$	σ (10^{-26} cm^2)	a_2	$\frac{\sigma(180)}{\sigma(90)}$
$(1+Px)/2$	1.18	Y	0	9.0	0	.77	0	.39	3.25	3.25	23.1	.15	1.26
$(1+Px)/2$	1.18	Y	5.6	9.9	0	.75	0	.04	2.91	2.91	-	-	-
$(1+Px)/2$	1.35	Y	0	9.3	0	.98	0	.57	4.6	4.6	22.9	.21	1.45
$(1+Px)/2$	1.35	Y	1.9	10.2	0	.78	0	.14	3.20	3.20	23.1	.24	1.46
$(.37+.63Px)S_{12}$*	1.35	Y	1.9	10.7	-.20	.70	.12	.12	3.04	2.95	-	-	-
$(.24+.76Px)S_{12}$*	1.35	Y	1.9	12.0	-.35	.66	.24	.06	2.61	2.46	-	-	-
$.45 + .55\ Px$	1.35	Y	1.9	10.3	-.16	.78	-.02	.15	3.52	2.84	-	-	-
$.4 + .6\ Px$	1.35	Y	1.9	10.4	-.32	.77	-.05	.16	3.78	2.48	-	-	-
$(1+Px)/2$	0.7	E	0	7.9	0	.99	0	.39	4.00	4.00	21.5	.17	1.30
$.45 + .55\ Px$	0.7	E	0	7.9	-.10	.99	-.07	.39	4.33	3.69	-	-	-
$.4 + .6\ Px$	0.7	E	0	8.0	-.20	1.00	-.16	.41	4.68	3.39	-	-	-
$(1+Px)/2$	0.75	E	1.8	8.7	0	.92	0	.03	3.8	3.8	21.7	.18	1.33
$-(\sigma_1 \cdot \sigma_2)(\tau_1 \cdot \tau_2)/3$	2.0	S	0	7.1	-.86	1.13	-.34	.12	9.57	1.59	21.3	.11	1.42
$-(\sigma_1 \cdot \sigma_2)(\tau_1 \cdot \tau_2)/3$	1.8	S	0	7.4	-.61	.63	-.19	.05	3.50	1.30	22.2	.04	1.14
EXPERIMENTAL VALUE				7.9 ± 1.0	$-.14 \pm .10$	$.68 \pm .10$	$.02 \pm .10$	$.11 \pm .10$	$3.6 \pm .6$	3.0 ± 1.0	19.4 ± 2.0	$.26 \pm .10$	$1.55 \pm .20$

* The exchange dependence for the central force is $(1+Px)/2$.

Table III

High energy scattering behavior of various models. In the above range (R) is the same in singlet and triplet states. For all cases where $\gamma \neq 0$, γ is adjusted to $Q = 2.73 \times 10^{-27}$ cm^2. σ is the total cross section, the differential cross section being $4\pi\sigma(\theta) = \sigma \cdot \sum a_n P_n(\theta)$, where $a_o = 1$.

Table IV

Properties of Selected Yukawa Potentials

Central range (10^{-13} cm)	Tensor range (10^{-13} cm)	γ	W_D	$^3\rho$ (10^{-13}cm)	^3r (10^{-13}cm)	^3T (10^{-39}cm^3)	^3a (10^{-13}cm)
1.18	1.18	5.6	5.3	1.56	1.48	.3	5.22
1.18	1.69	0.8	3.2	1.71	1.49	1.0	5.29
1.18	1.98	0.5	2.8	1.76	1.50	1.2	5.30
1.18	3.91	0.16	1.7	1.90	1.45	2.1	5.35
1.18	(No tensor force)	-	-	1.67	1.54	.6	5.29
1.35	1.35	1.91	4.2	1.71	1.58	.55	5.32
1.35	(No tensor force)	-	-	1.85	1.63	.96	5.39

In the above $^3\rho$ is the effective range as determined by using the deuteron wave function. ^3T, the shape dependent coefficient, has been determined from the approximate relation $^3T = \frac{1}{4}(^3r)^2(^3\rho - {}^3r)$, and checked by neglecting in the exact expression for ^3T all terms involving the coupled D state[9]. All the above potentials gave a value of 0.28 (within 2 percent) for the ratio of the cross sections for photomagnetic to photoelectric disintegrations of the deuteron for the 2.76 Mev Na γ-ray using a value of 2.23 Mev as the binding energy of the deuteron. [For experimental values see W. M. Woodward and I. Halpern, Phys. Rev. 76, 107 (1949); E. Meiners, Phys. Rev. 76, 259 (1949).]

Table V

Comparison of Contributions of Various States to Total Cross Section

State	Square well		Yukawa	
	Tensor forces (10^{-26} cm^2)	Central forces (10^{-26} cm^2)	Tensor forces (10^{-26} cm^2)	Central Forces (10^{-26} cm^2)
$^3S_1$	2.95^+	3.25^+	8.82^+	9.58^+
$^3D_1$	0.35^-	0.95^+	0.55^-	0.14^+
$^3D_2$	5.87^+	1.58^+	1.82^+	0.24^+
$^3D_3$	0.72^+	2.21^+	0.14^-	0.33^+

Table VI

Singlet phase shifts at 20 and 32 Mev for various radial forms adjusted to fit the low energy scattering.

Model	V_c	R	Phase shift 32 Mev S	32 Mev D	20 Mev S*	20 Mev D
$V_c(r/R)=\begin{cases} V_c & r<R \\ 0 & r>R \end{cases}$	13.273 Mev	2.615×10^{-13} cm	41.99°	0.770°	48.5°	0.26°
$V_c(r/R)=V_c e^{-r/R}$	108.27 Mev	0.7088×10^{-13} cm	47.54°	1.20°		
$V_c(r/R)=\frac{V_c e^{-r/R}}{r/R}$	49.350 Mev	1.1417×10^{-13} cm	51.15°	1.40°	54.2°	0.7°

* Interpolated

Figures

Fig. 1 Experimental angular distribution. The circles are the counter data [see Hadley, Kelly, Leith, Segrè, Wiegand, and York, Phys. Rev. 75, 351 (1949) and Kelly, Leith Segrè, and Wiegand, Phys. Rev. 79, 96 (1950).]. The horizontal lines at 90 Mev are the result of the cloud chamber measurements. [See Brueckner, Hartsough, Hayward, and Powell, Phys. Rev. 75, 555 (1949).] The crosses at 90 Mev covering the angular range from 25° to 74° were determined by a photographic plate technique. [R. Wallace, Phys. Rev., in press.] The triangle at 90 Mev covering the angular range from 130° to 180° were determined by scintillation counter technique. [R. H. Fox, Phys. Rev., in press.] The normalization chosen agrees with the total cross section as given in Table II. The dashed line represents the best fit as determined from the expansion in Legendre polynomials. [See Table III.]

Fig. 2 (Energy) x (total cross section) vs. energy. The full curve indicates the general characteristics of a potential model having a singular behavior at the origin such as Yukawa radial dependence.

Fig. 3 The triplet effective range for the Yukawa (Y), exponential (E), and the square well (S) potentials. The intrinsic range is 2.12 R, 3.54 R, and R for the three potentials in the order named above. R is the usual parametric range that occurs in the radial dependence, i.e., $\exp(-r/R)/(r/R)$, $\exp(r/R)$ for the Yukawa and exponential potentials and a constant potential extending a distance R for the square well potential.

Fig. 4 Low energy triplet scattering on the assumption of a 3.0×10^{-13} cm singlet effective range. This plot yields $5.51 \pm 0.16 \times 10^{-13}$ cm and $1.98 \pm 0.26 \times 10^{-13}$ cm for the triplet scattering length and effective range, respectively. The experimental points [open circles, (Bailey, Bennett, Bergstralh, Nuckolls, Richards, and Williams, Phys. Rev. 70, 583 (1946)), solid circles (Professor J. H. Williams has kindly communicated to us more recent values of the experiments of Lampi, Freier, and Williams, Phys. Rev. 76, 188 (1949). Further experiments are still in progress.)] are from the data of the Minnesota group.

Fig. 5 Triplet S wave scattering at 90 Mev.

Fig. 6 Central force scattering at 40 and 90 Mev. The first column gives the triplet scattering; the second, the singlet scattering; and the third, the complete scattering (assuming equal intrinsic ranges). The first row is for the square well; the second, for the exponential; and the third, for the Yukawa potential. In each figure the upper set of three curves is for 40 Mev; the lower, for 90 Mev. For each set of three curves the uppermost is $4\pi\cdot\sigma(180°)$; the middle curve is

the total cross section; and the lower is $4\pi\cdot\sigma(90^\circ)$. (Illustrated in the first figure by A, B, and C, respectively.) In all cases the exchange dependence is assumed to be $\frac{1}{2}(1 + P_x)$ [therefore, $\sigma(180^\circ) = \sigma(0^\circ)$], and the depths are chosen to fit the deuteron and the zero energy scattering.

Fig. 7. S wave scattering phase shift, illustrated for a triplet effective range of 1.65×10^{-13} cm and a singlet effective range of 3.0×10^{-13} cm. Y, E, and S refer to the Yukawa, exponential, and square well central potentials, respectively. The experimental points below 25 Mev are from the data of W. Sleator, Jr., Phys. Rev. 72, 207 (1947), and R. Sherr, Phys. Rev. 68, 240 (1945) (above 40 Mev, see Table II).

Fig. 8 D. wave scattering. The quantity plotted is the sine of the D wave phase shift for the singlet and triplet Yukawa (labeled ^{1}Y and ^{3}Y) and for the singlet and triplet square well potentials (labeled ^{1}S and ^{3}S).

Fig. 9 Scattering at 40 and 90 Mev from an exponential potential, $\exp(-r/R)$, ($R = 0.7 \times 10^{-13}$ cm for both singlet and triplet states) without tensor force. The solid lines are for a $(1 + P_x)/2$ exchange dependence; the dotted curves illustrate the effect of increasing the amount of exchange forces. The total cross sections for this potential are 21.7×10^{-26} cm^2 and 7.9×10^{-26} cm^2 at 40 and 90 Mev, respectively. The experimental points (see Fig. 1) have been normalized to fit the theoretical angular distribution.

Fig. 10 Scattering from the Yukawa potential $\exp(-r/R)/(r/R)$ at 40 and 90 Mev for a range $R = 1.35 \times 10^{-13}$ cm for both singlet and triplet states without tensor force. The total cross sections are 22.9 and 9.3×10^{-26} cm^2 at 40 and 90 Mev respectively.

Fig. 11 Quadrupole moment for the square well. The binding energy used is 2.23 Mev, and the tensor and central ranges, R, are equal. b is the customary dimensionless well depth, equal to $MV_cR^2/\hbar$.

Fig. 12 Quadrupole moment for the Yukawa well. (The results for $R = 1.185 \times 10^{-13}$ cm are in agreement with those from more precise calculations communicated to the author by H. Feshbach.) The binding energy used is 2.183 Mev, and the tensor and central ranges, R, are equal. b is the customery dimensionless well depth, equal to $MV_cR^2/\hbar$. The curve for $R = 1.120 \times 10^{-13}$ cm, shown as dashed, is extrapolated.

Fig. 13 Ratio of central well depth to tensor well depth for quadrupole moment equal to 2.73×10^{-27} cm^2. The binding energy fitted for the Yukawa (Y) case is 2.183 Mev and for the square well (S) case is 2.23 Mev.

Fig. 14 Low energy scattering with tensor forces for the Yukawa (Y) and the square well (S) potentials. The range, R, is indicated (in units of 10^{-13} cm) parametrically along the curves. (Depths are adjusted to fit the binding energy and the quadrupole moment of the deuteron.)

Fig. 15 Variation of deuteron fitting parameters for increase of tensor range. The interaction is that of the Yukawa well for which the central range is 1.185×10^{-13} cm. W_D is the percentage of D state; b is the dimensionless central well depth equal to $MV_cR^2/\hbar$; γb is the tensor well depth. The binding energy fitted is 2.183 Mev.

Fig. 16 Effect of increasing the tensor depth (at 90 Mev) with constant binding energy illustrated for a Yukawa potential ($R = 1.18 \times 10^{-13}$ cm). Curve I: $\gamma = 0$, triplet cross section $= 9.9 \times 10^{-26}$ cm^2. Curve II: $\gamma = 0.5$, triplet cross section $= 9.6 \times 10^{-26}$ cm^2. Curve III: $\gamma = 6$, triplet cross section, $= 11.1 \times 10^{-26}$ cm^2.

Fig. 17 Scattering from the Yukawa potential ($R = 1.35 \times 10^{-13}$ cm) at 40, 90, and 280 Mev with inclusion of tensor force. The total cross sections are 23.1×10^{-26} cm^2, 9.8×10^{-26} cm^2 and 3.7×10^{-26} cm^2.

Fig. 18 Scattering from the exponential potential ($R = 0.75 \times 10^{-13}$ cm) at 40 and 90 Mev with inclusion of tensor force. The total cross sections are 21.7×10^{-26} cm^2 at 40 Mev and 8.7×10^{-26} cm^2 at 90 Mev.

Fig. 19 Effect of increasing the tensor range (at 90 Mev) with constant binding energy and quadrupole moment illustrated for a Yukawa potential (central range $= 1.18 \times 10^{-13}$cm). Curve I: Tensor range $= 1.18 \times 10^{-13}$ cm, complete cross section $= 9.9 \times 10^{-26}$ cm^2. Curve II: Tensor range $= 1.69 \times 10^{-13}$ cm, complete cross section $= 10.5 \times 10^{-26}$ cm^2. Curve III: Tensor range $= 3.91 \times 10^{-13}$ cm, complete cross section $= 10.7 \times 10^{-26}$ cm^2.

Fig. 20 The 27.2 Mev angular distribution. [See Brolley, Coon, and Fowler, Phys. Rev. 79, 227 (1950).] The solid line is the theoretical prediction of the Yukawa tensor model.

Fig. 21 Comparison of n-p and p-p scattering data.

Fig. 22 Effects of S, D, and P waves on 32 Mev scattering. The upper set of curves give the nuclear scattering. The lower set include the effects of Coulomb forces.

Fig. 23 Tensor scattering from a singular potential at various energies. The energies in Mev are given parametrically on the curves.

Fig. 24 Effect of adding tensor scattering to the singlet scattering at 32 Mev. A. Nuclear scattering. B. Scattering including the effects of Coulomb forces. The tensor scattering is that from a poential of exponential radial dependence ($R = 0.71 \times 10^{-13}$ cm, $V_t = \pm 50$ Mev).

Fig. 25 Singlet scattering at 350 Mev as predicted for a potential having Yukawa radial dependence $R = 1.1416 \times 10^{-13}$ cm and (II) for a square well potential $R = 2.615 \times 10^{-13}$ cm.

Fig. 26 Comparison of exact and Born calculations for tensor force scattering at 32 Mev from a potential of Yukawa radial dependence ($R = 1.25 \times 10^{-13}$ cm).

Fig. 27 Comparison of exact and Born calculations for tensor force scattering at 350 Mev from a potential of Yukawa radial dependence ($R = 1.25 \times 10^{-13}$ cm).

Fig. 28 Singlet scattering at 32 Mev from potentials with various radial forms adjusted to fit the low energy scattering. Data taken from reference 11 (29.4 Mev) and 12 (31.8 Mev).

Fig. 29 P wave scattering added to the singlet scattering predicted by the Yukawa potential at 32 Mev.

Fig. 30 Total scattering at 32 Mev by singlet and triplet tensor potentials of the same radial form. (The singlet potentials have range and depth adjusted to fit the low energy scattering). A. Square. B. Exponential. C. Yukawa. Data taken from reference 12 (31.8 Mev).

Fig. 31 Best fit at 32 Mev compared to S wave and singlet scattering at 32 and 20 Mev. I. Singlet square well $R = 2.615 \times 10^{-13}$ cm and depth 13.273 Mev; triplet tensor Yukawa potential $R = 1.25 \times 10^{-13}$ cm and $V_t = 23$ Mev (or $S_{12}V_t \exp(-r/R)/(r/R)^2$ with $R = 1.6 \times 10^{-13}$ cm and $V_t = 18$ Mev). II. S wave scattering. III. Singlet scattering from Yukawa potential $R = 1.1417 \times 10^{-13}$ cm and $V_c = 49.350$ Mev; no tensor forces.

Fig. 32 Born tensor scattering amplitude for various potentials. The abscissa scale has been adjusted so that all potentials will give the same angular distribution at 32 Mev as the Yukawa potential with $R = 1.25 \times 10^{-13}$ cm for a suitable choice of depth.

Fig. 33 Complete cross section at 350 Mev for various tensor models adjusted to fit the 32 Mev data. The legend shows the tensor model used. Data taken from reference 13.

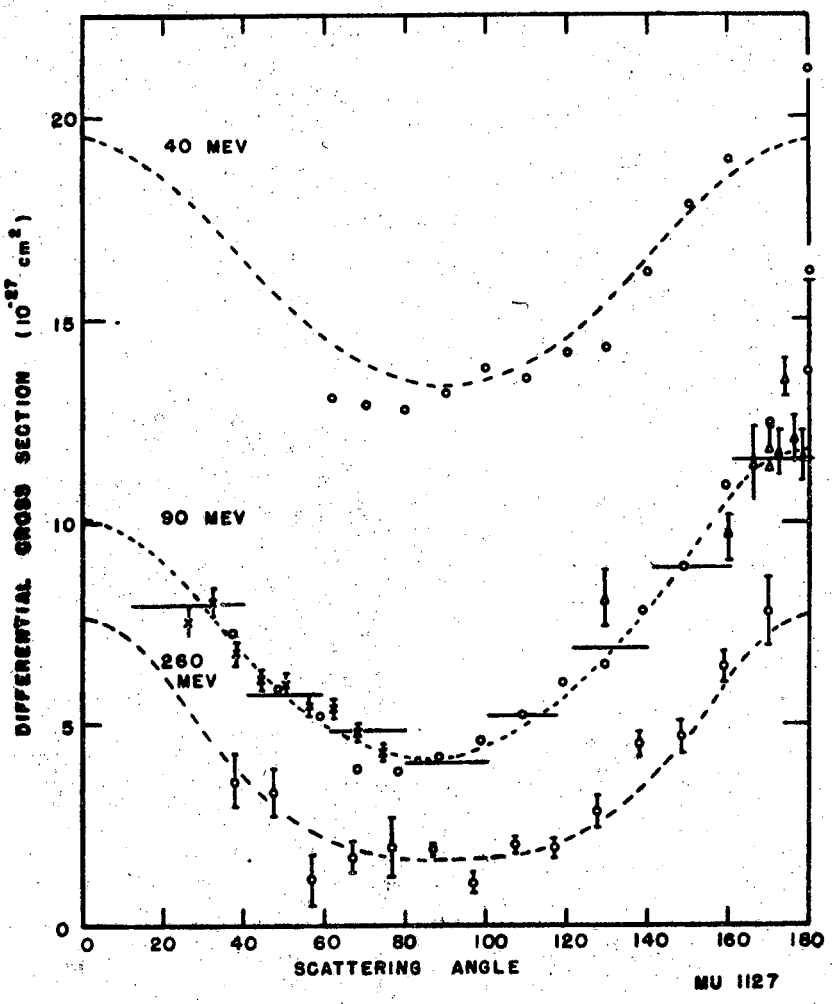
40 MEV
90 MEV
260 MEV
DIFFERENTIAL CROSS SECTION (10^-27 cm^2)
SCATTERING ANGLE
0
5
10
15
20
0
20
40
60
80
100
120
140
160
180
MU 1127

Fig. 1

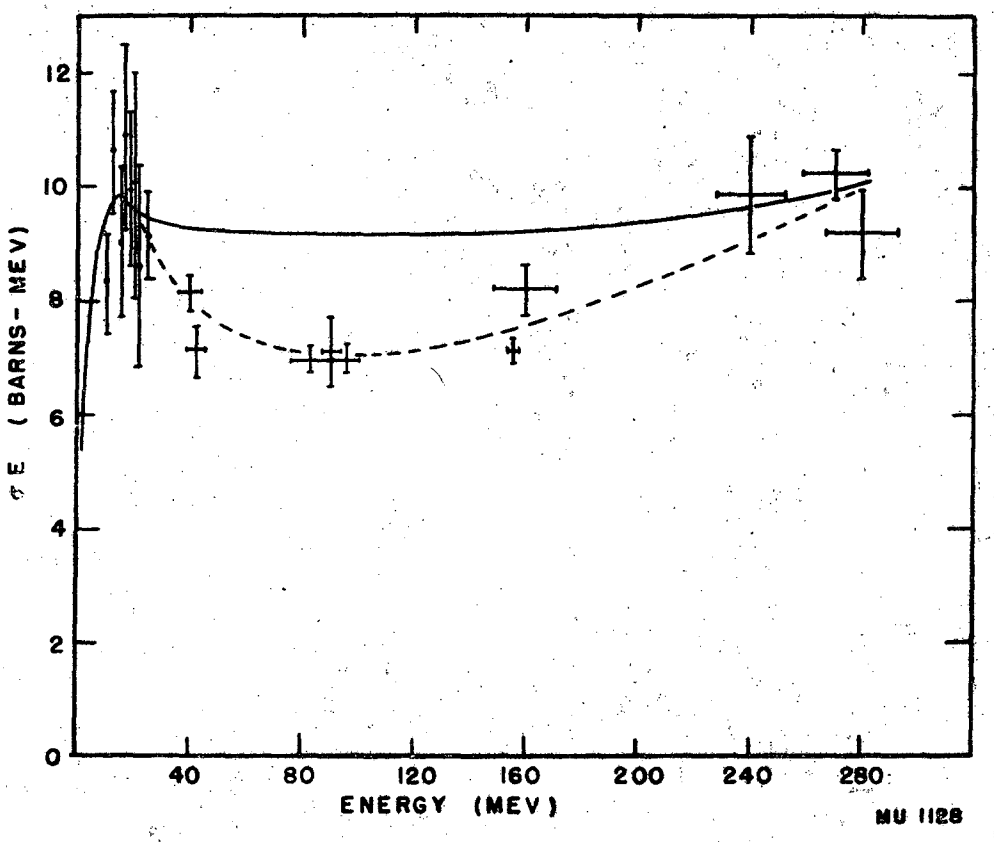
σE (BARNS-MEV)
0
2
4
6
8
10
12
40
80
120
160
200
240
280
ENERGY (MEV)
MU 1128

Fig. 2

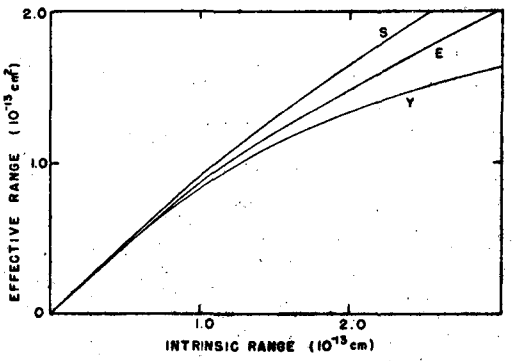
2.0
1.0
0
S
E
Y
EFFECTIVE RANGE (10^{-13} cm)
1.0
2.0
INTRINSIC RANGE (10^{-13} cm)

Fig. 3

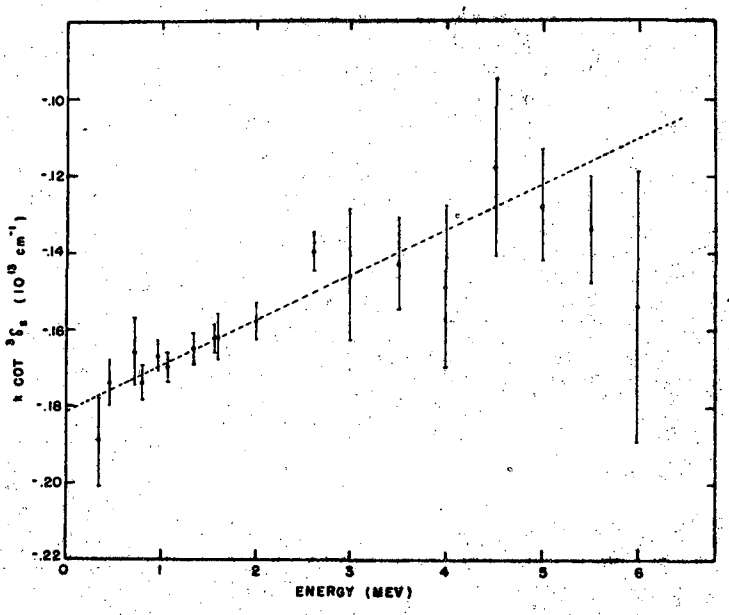
-.10
-.12
-.14
-.16
-.18
-.20
-.22
k COT $^3\delta_0$ (10^{13} cm^{-1})
0
1
2
3
4
5
6
ENERGY (MEV)

Fig. 4

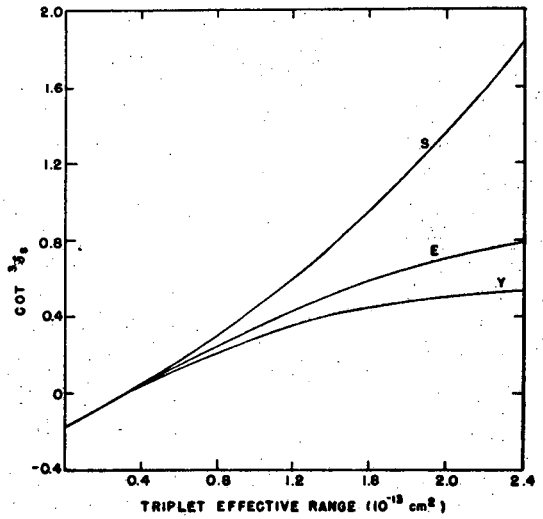
2.0
1.6
1.2
0.8
0.4
0
-0.4
COT $^3S_0$
S
E
V
0.4
0.8
1.2
1.8
2.0
2.4
TRIPLET EFFECTIVE RANGE (10^{-13} cm^2)

Fig. 5

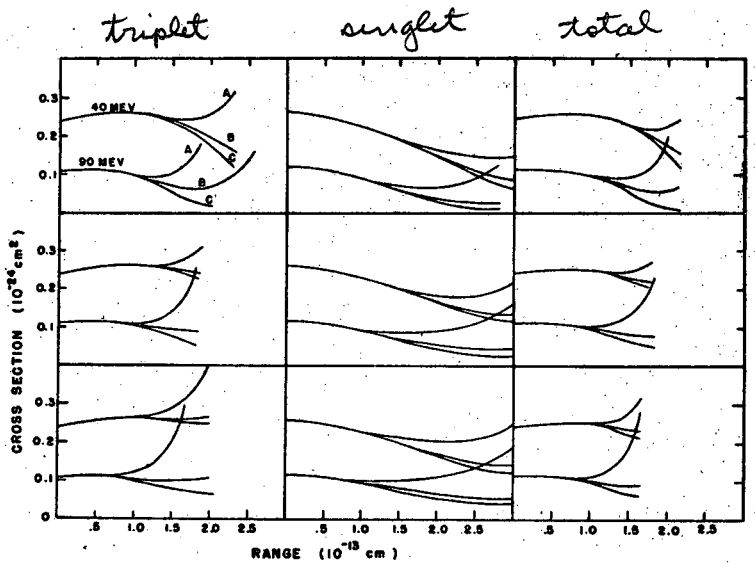
triplet
singlet
total
40 MEV
90 MEV
A
B
C
A'
B'
C'
CROSS SECTION (10^{-26} cm^2)
RANGE (10^{-13} cm)
.5
1.0
1.5
2.0
2.5
square well
exponential well
yukawa well

Fig. 6

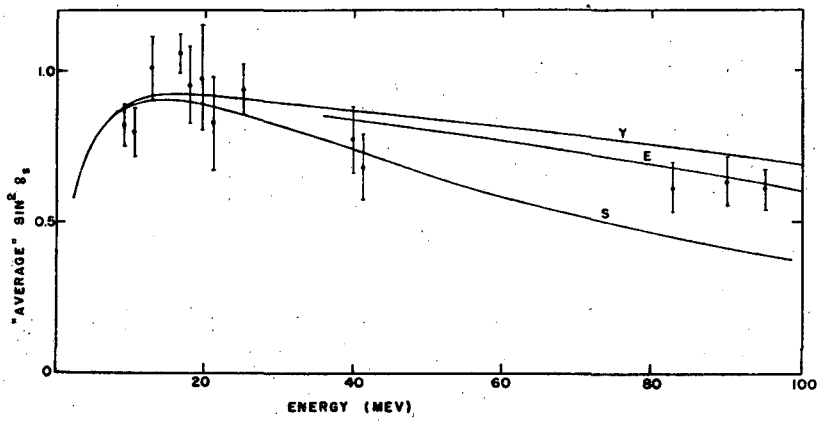
1.0
0.5
0
"AVERAGE" SIN² δ₀
20
40
60
80
100
ENERGY (MEV)
Y
E
S

Fig. 7

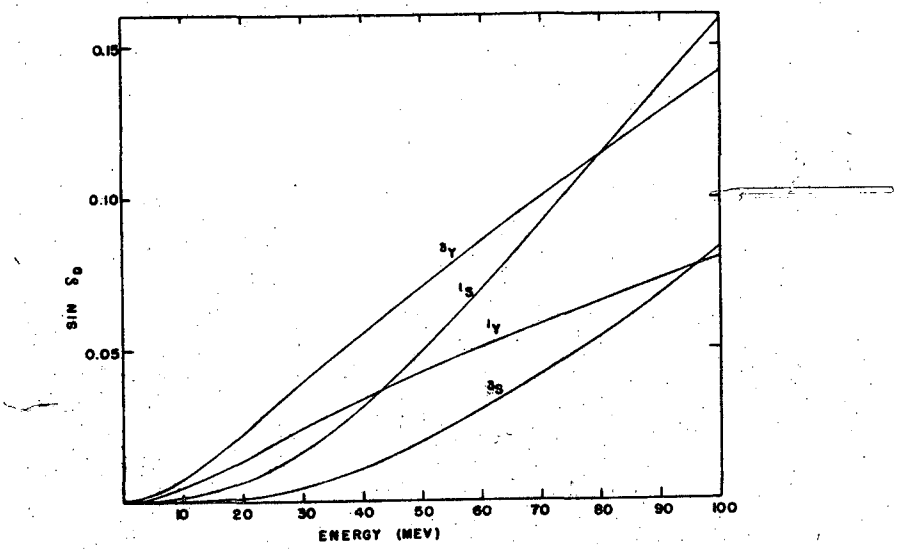
0.15
0.10
0.05
SIN δ₀
10
20
30
40
50
60
70
80
90
100
ENERGY (MEV)
³Y
¹S
¹Y
³S

Fig. 8

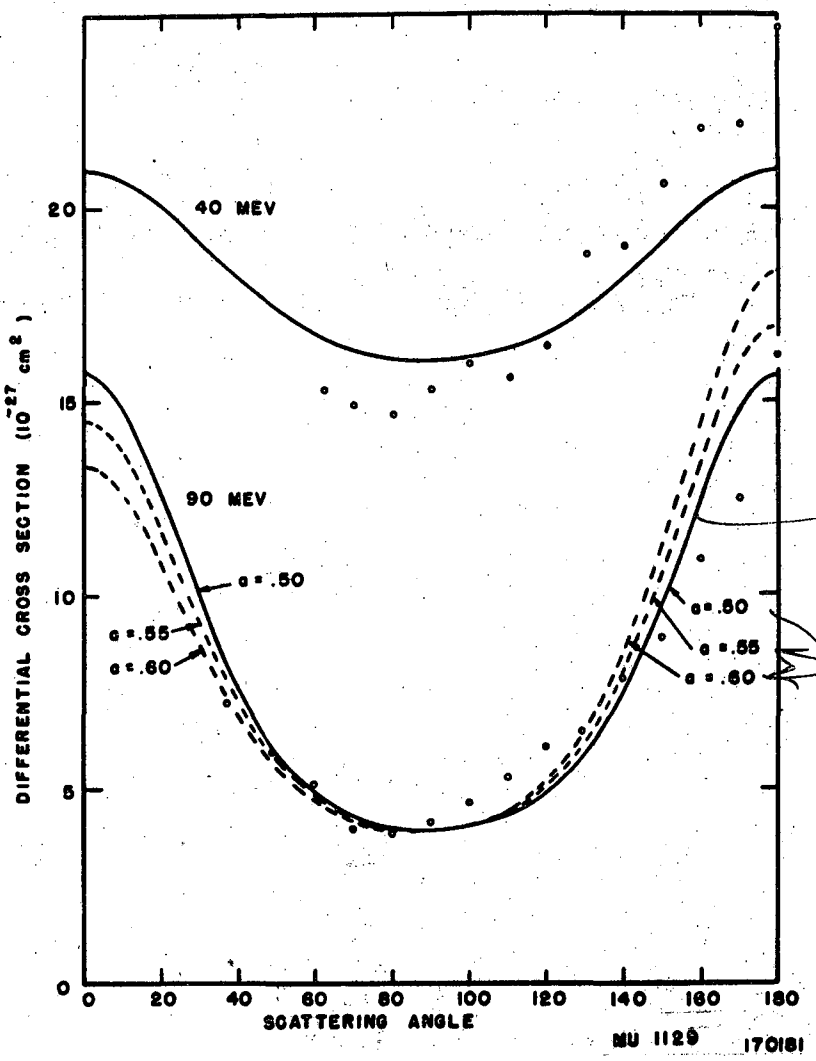

Exponential Well

$\frac{1+P}{2}$

fraction of exchange force.

Fig. 9

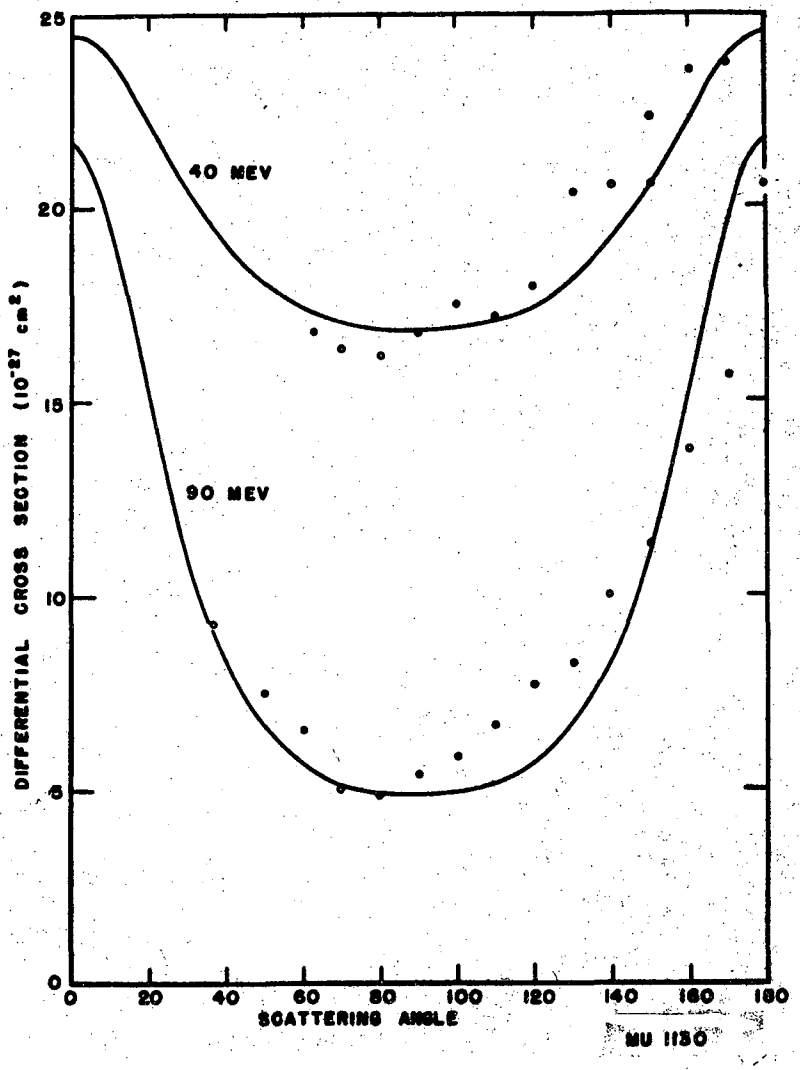

Yukawa Well

Fig. 10

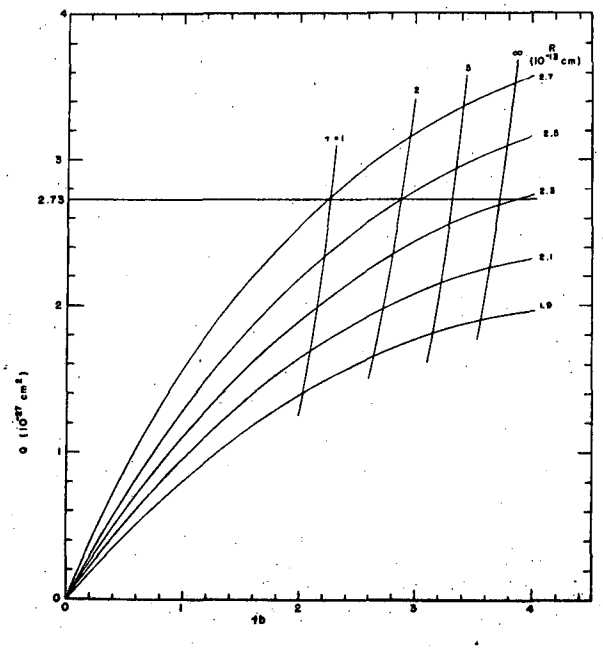
R
(10^13 cm)
∞
2.7
2.5
2.3
2.1
1.9
2.73
τ=1
2
5
Q (10^27 cm^2)
τb

Fig. 11

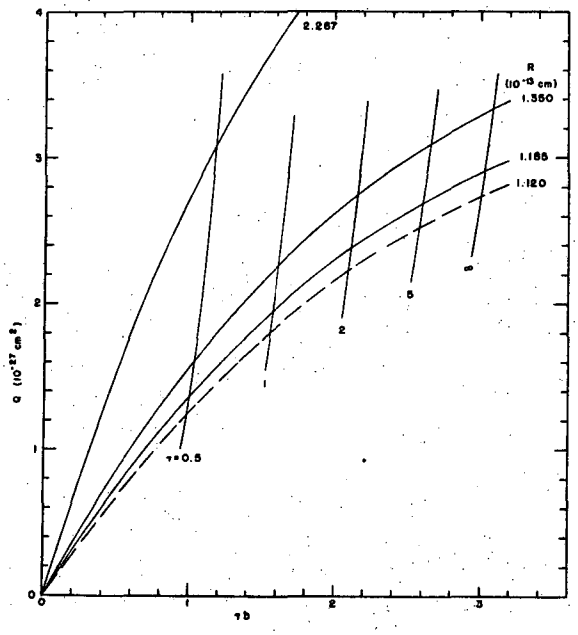
2.267
R
(10^13 cm)
1.350
1.185
1.120
τ=0.5
1
2
5
8
Q (10^27 cm^2)
τb

Fig. 12

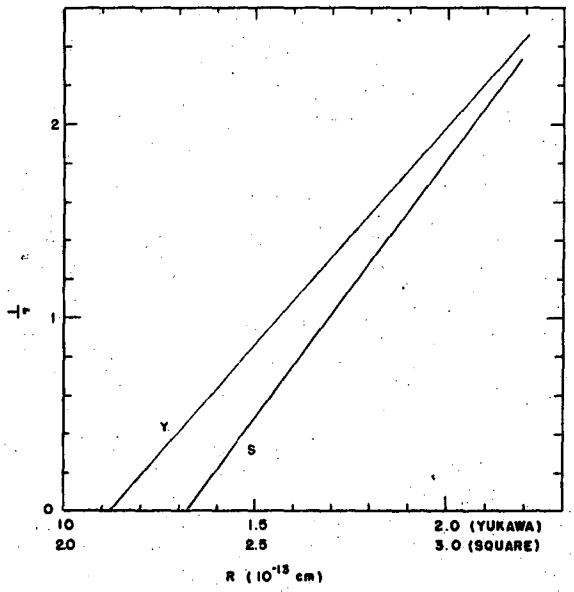
2
1
0
Y
S
1.0
2.0
1.5
2.5
2.0 (YUKAWA)
3.0 (SQUARE)
R (10^-13 cm)

Fig. 13

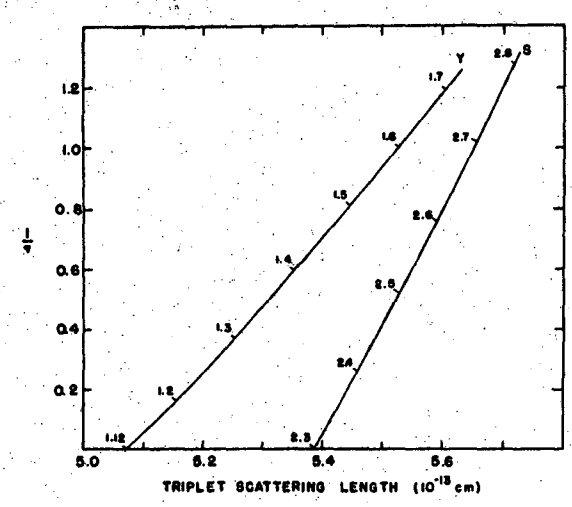
1.2
1.0
0.8
0.6
0.4
0.2
5.0
5.2
5.4
5.6
Y
S
1.7
1.6
1.5
1.4
1.3
1.2
1.12
2.8
2.7
2.6
2.5
2.4
2.3
TRIPLET SCATTERING LENGTH (10^-13 cm)

Fig. 14

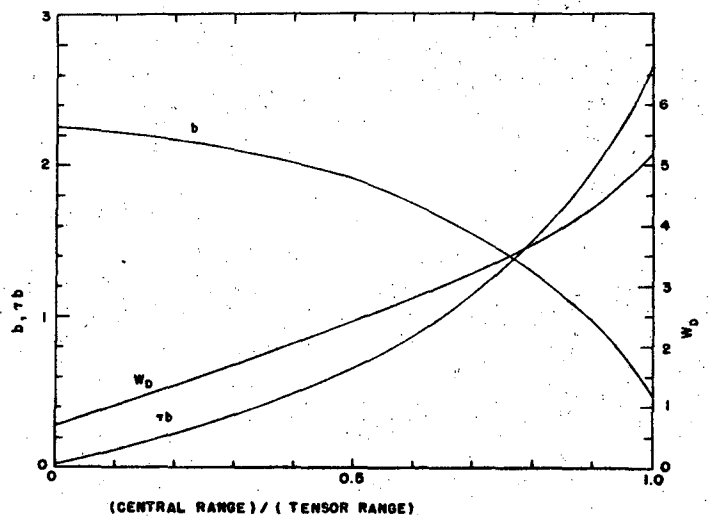
b
W_D
τb
b, τ b
W_D
(CENTRAL RANGE) / (TENSOR RANGE)

Fig. 15

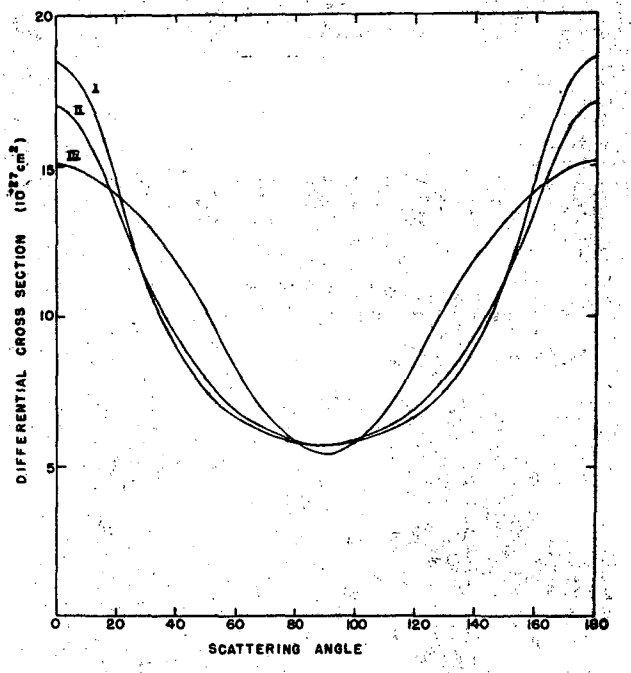
I
II
III
DIFFERENTIAL CROSS SECTION (10^{-27} cm^2)
SCATTERING ANGLE

Fig. 16

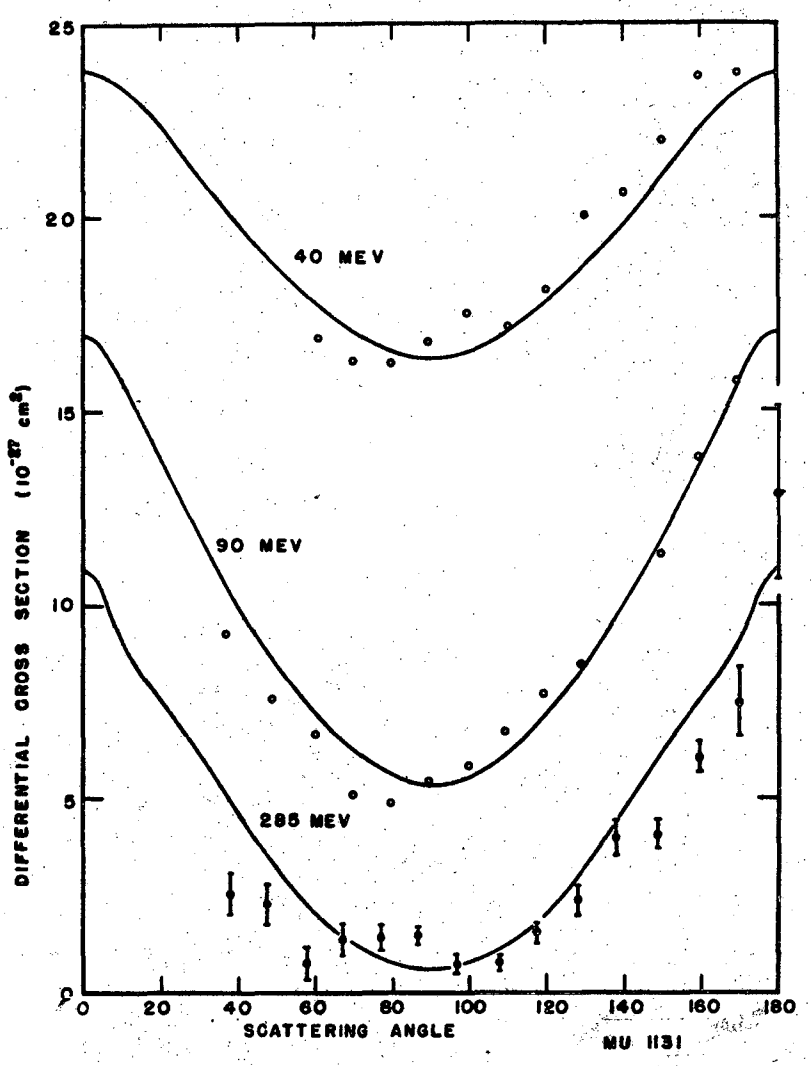
25
20
15
10
5
0
40 MEV
90 MEV
285 MEV
DIFFERENTIAL CROSS SECTION (10⁻²⁷ cm²)
0
20
40
60
80
100
120
140
160
180
SCATTERING ANGLE
MU 1131

Fig. 17

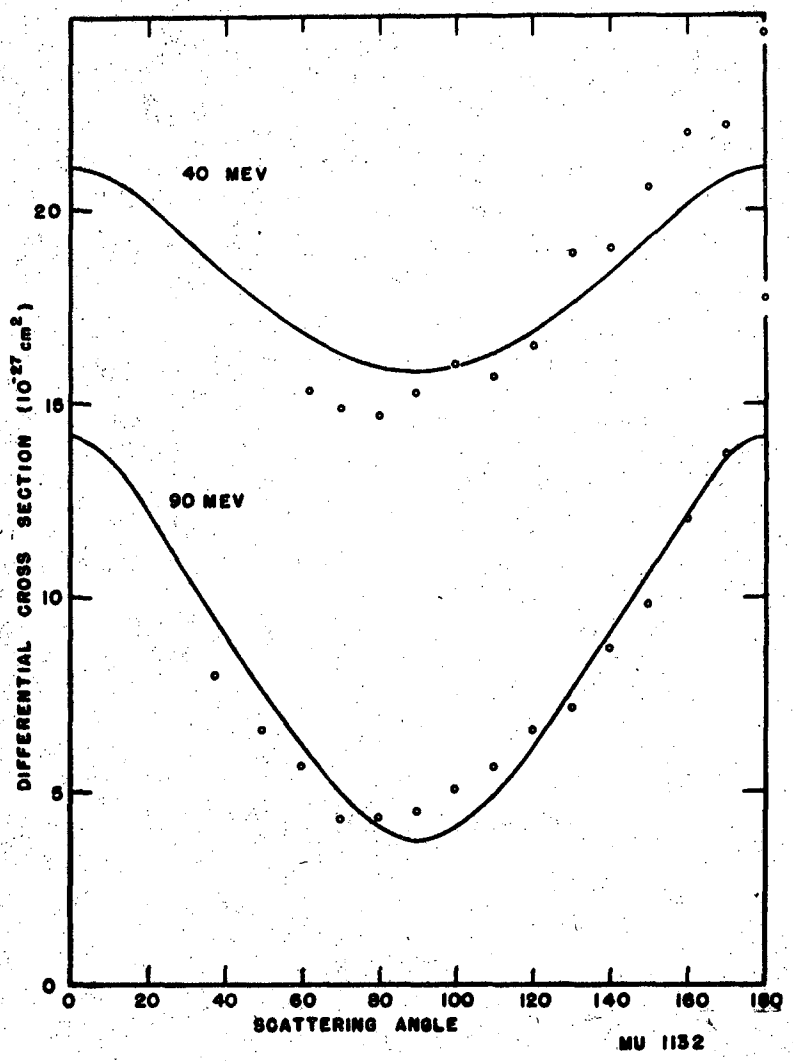
40 MEV
90 MEV
DIFFERENTIAL CROSS SECTION (10^{-27} cm^2)
SCATTERING ANGLE
0
5
10
15
20
0
20
40
60
80
100
120
140
160
180
MU 1132

Fig. 18

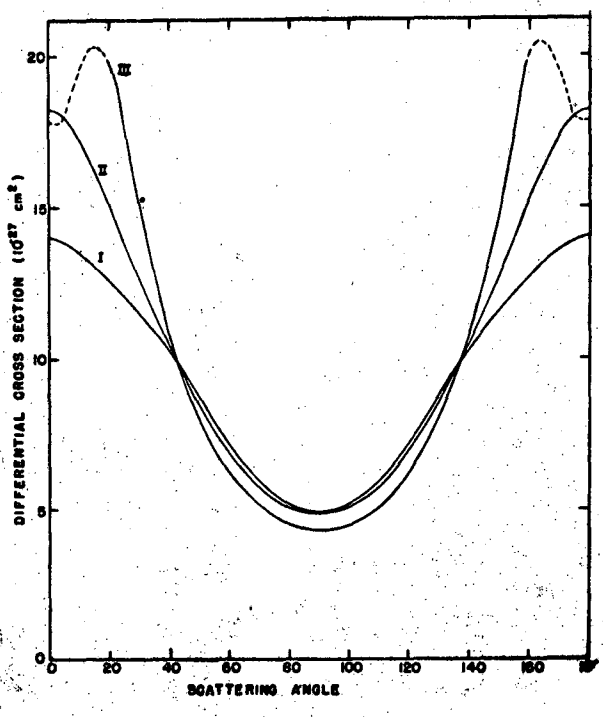
DIFFERENTIAL CROSS SECTION (10^{27} cm^2)
SCATTERING ANGLE
0
5
10
15
20
0
20
40
60
80
100
120
140
160
I
II
III

Fig. 19

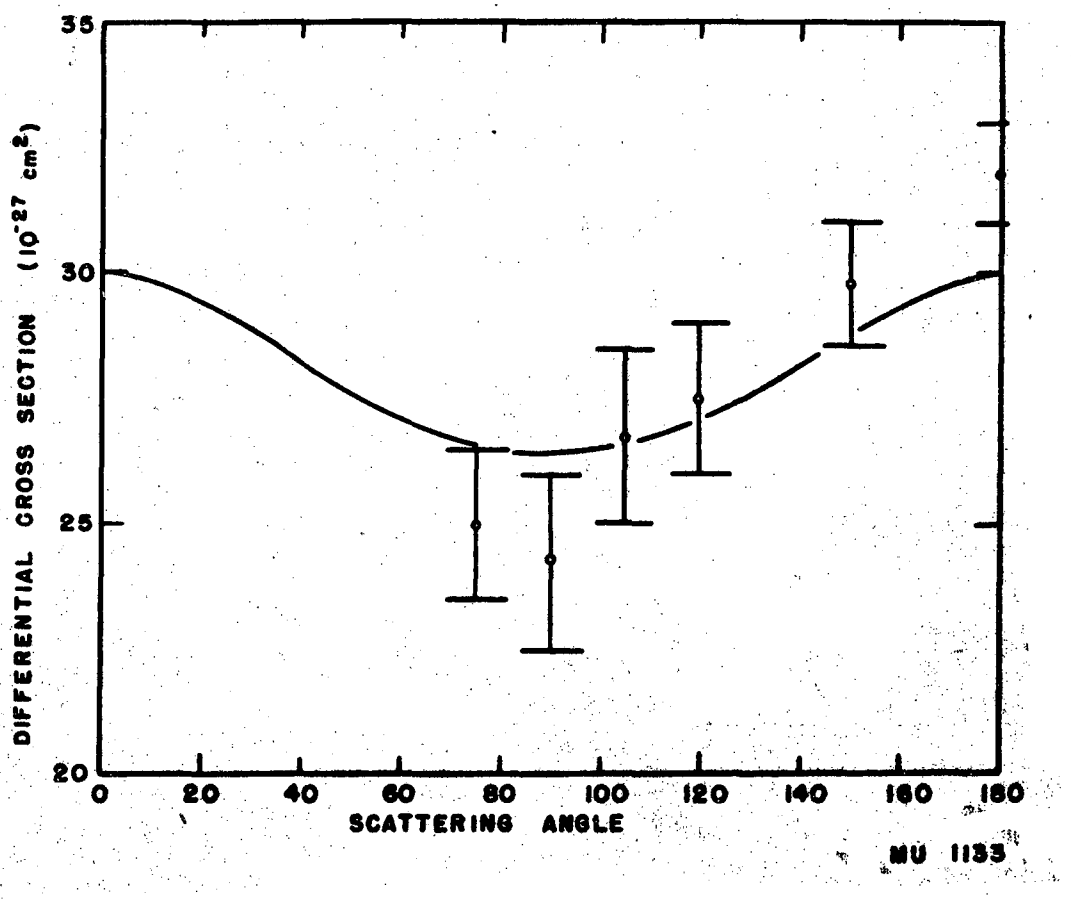
35
30
25
20
DIFFERENTIAL CROSS SECTION (10^-27 cm^2)
0
20
40
60
80
100
120
140
160
180
SCATTERING ANGLE
MU 1135

Fig. 20

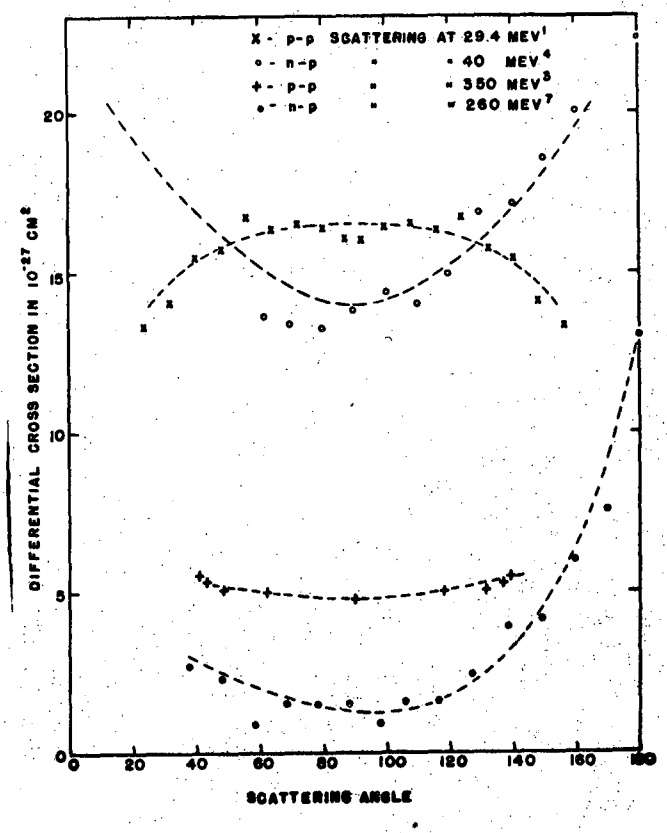
X - p-p SCATTERING AT 29.4 MEV[1]
o - n-p " " 40 MEV[4]
+ - p-p " " 350 MEV[5]
• - n-p " " 260 MEV[7]
DIFFERENTIAL CROSS SECTION IN 10^{-27} CM^2
SCATTERING ANGLE
0
5
10
15
20
0
20
40
60
80
100
120
140
160
180

Fig. 21

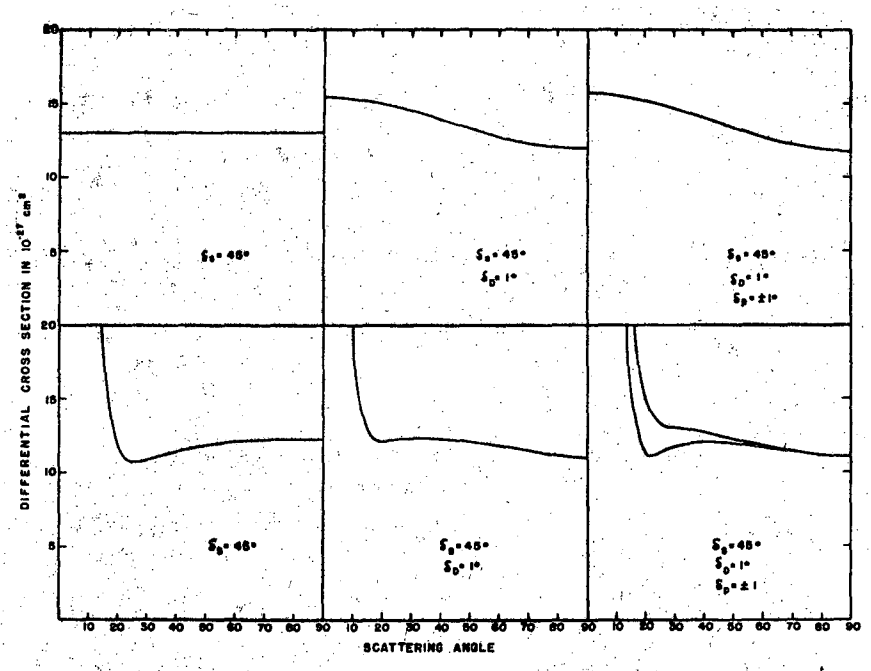
DIFFERENTIAL CROSS SECTION IN 10^{-27} cm^2
$\delta_s = 45°$
$\delta_s = 45°$ $\delta_0 = 1°$
$\delta_s = 45°$ $\delta_0 = 1°$ $\delta_p = \pm 1°$
$\delta_s = 45°$
$\delta_s = 45°$ $\delta_0 = 1°$
$\delta_s = 45°$ $\delta_0 = 1°$ $\delta_p = \pm 1$
SCATTERING ANGLE

Fig. 22

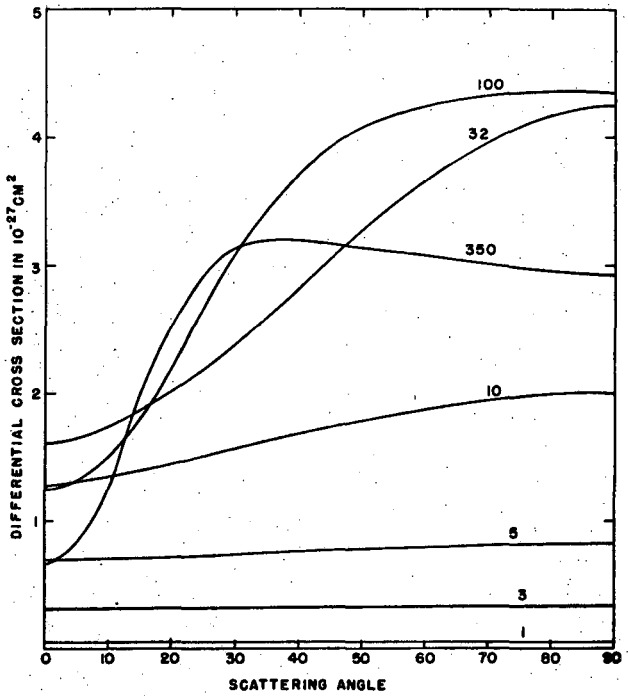
DIFFERENTIAL CROSS SECTION IN 10^{-27} CM^2
SCATTERING ANGLE
100
32
350
10
5
3
1

Fig. 23

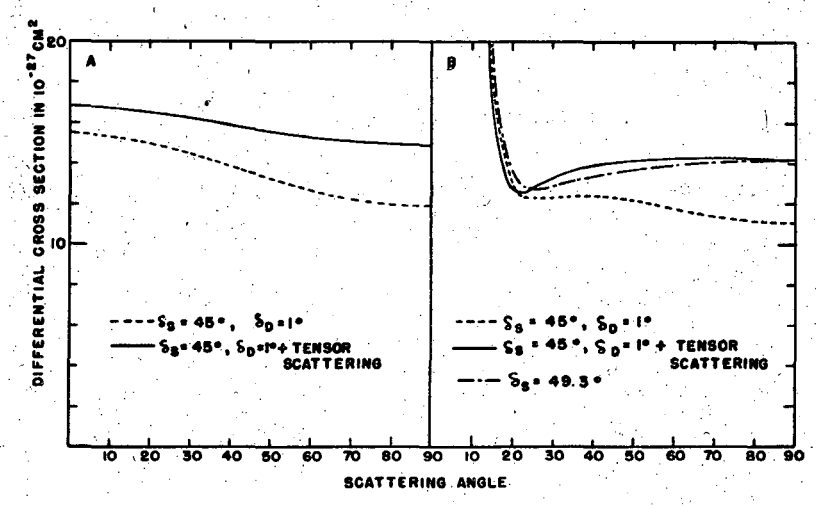
DIFFERENTIAL CROSS SECTION IN 10^{-27} CM^2
SCATTERING ANGLE
A
B
$\delta_S = 45°$, $\delta_D = 1°$
$\delta_S = 45°$, $\delta_D = 1°$ + TENSOR SCATTERING
$\delta_S = 49.3°$

Fig. 24

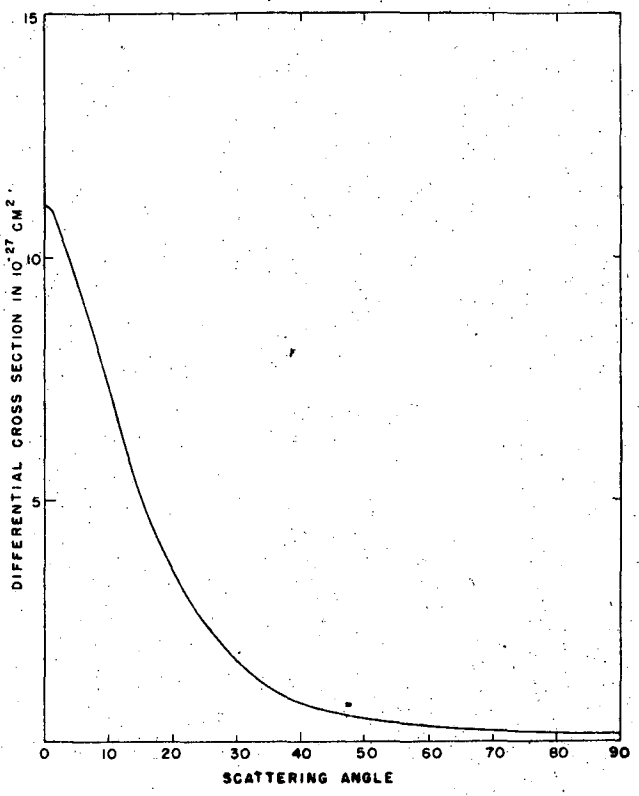
DIFFERENTIAL CROSS SECTION IN 10^{-27} CM^2
15
10
5
0
10
20
30
40
50
60
70
80
90
SCATTERING ANGLE

Fig. 25

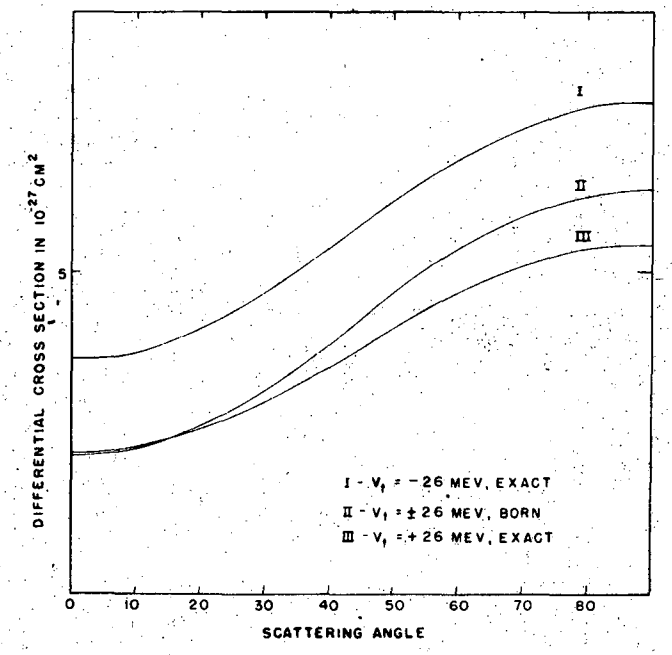
DIFFERENTIAL CROSS SECTION IN 10^{-27} CM^2
5
I
II
III
I - V_1 = −26 MEV, EXACT
II - V_1 = ±26 MEV, BORN
III - V_1 = +26 MEV, EXACT
0
10
20
30
40
50
60
70
80
SCATTERING ANGLE

Fig. 26

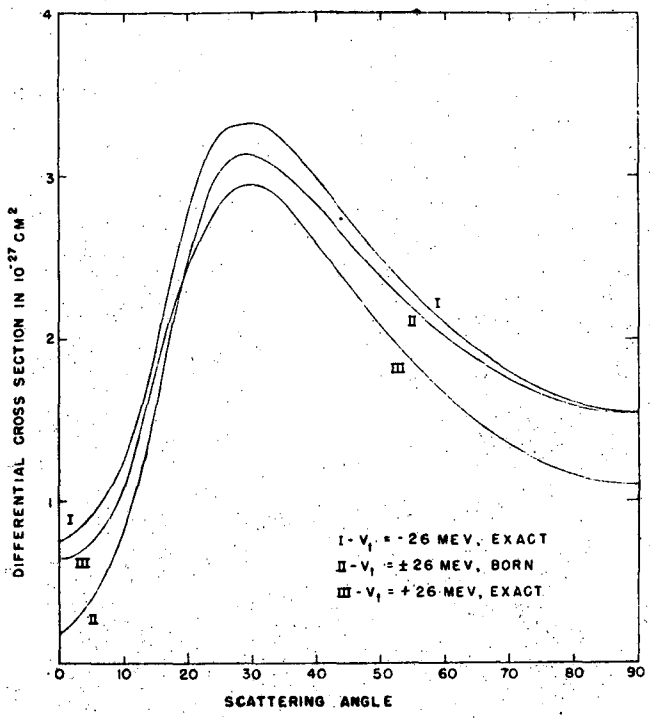
DIFFERENTIAL CROSS SECTION IN 10^{-27} CM^2
SCATTERING ANGLE
I - V_1 = - 26 MEV, EXACT
II - V_1 = ± 26 MEV, BORN
III - V_1 = + 26 MEV, EXACT

Fig. 27

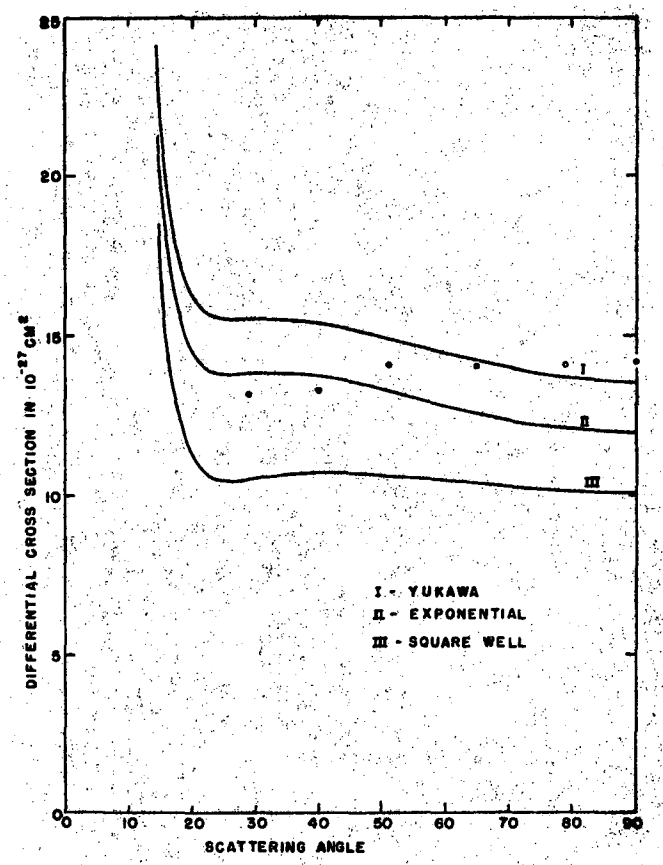
DIFFERENTIAL CROSS SECTION IN 10^{-27} CM^2
SCATTERING ANGLE
I - YUKAWA
II - EXPONENTIAL
III - SQUARE WELL

Fig. 28

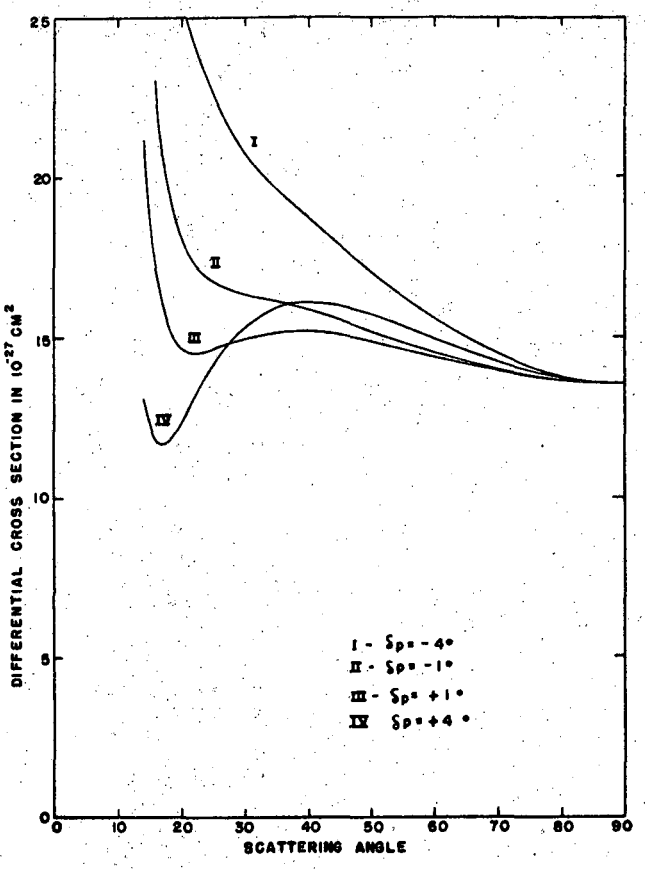
DIFFERENTIAL CROSS SECTION IN 10^{-27} CM^2
SCATTERING ANGLE
I - δ_p = - 4°
II - δ_p = - 1°
III - δ_p = + 1°
IV δ_p = + 4 °

Fig. 29

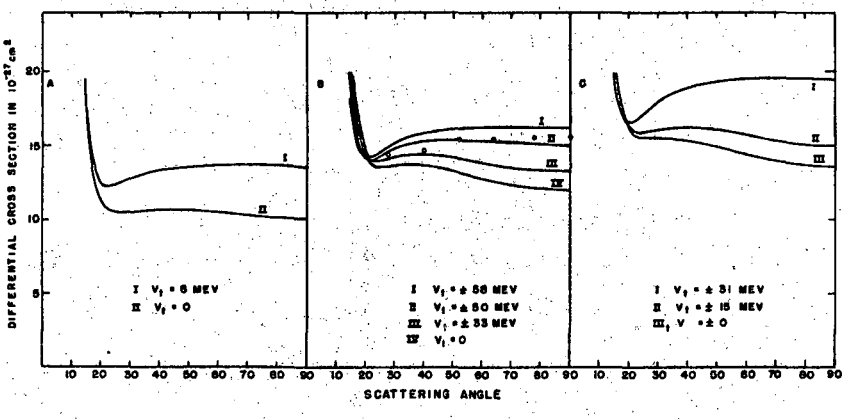
DIFFERENTIAL CROSS SECTION IN 10^{-27} cm^2
SCATTERING ANGLE
A
I V_t = 6 MEV
II V_t = 0
B
I V_t = ± 56 MEV
II V_t = ± 50 MEV
III V_t = ± 33 MEV
IV V_t = 0
C
I V_t = ± 31 MEV
II V_t = ± 15 MEV
III V_t = ± 0

Fig. 30

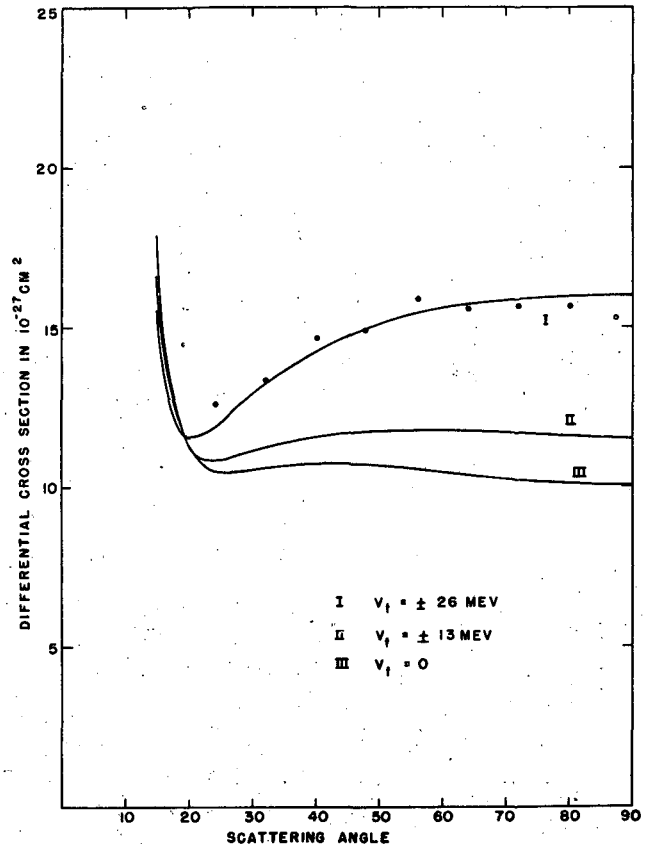
DIFFERENTIAL CROSS SECTION IN 10^{-27} CM^2
SCATTERING ANGLE
I $V_f = \pm$ 26 MEV
II $V_f = \pm$ 13 MEV
III $V_f = 0$

Fig. 31

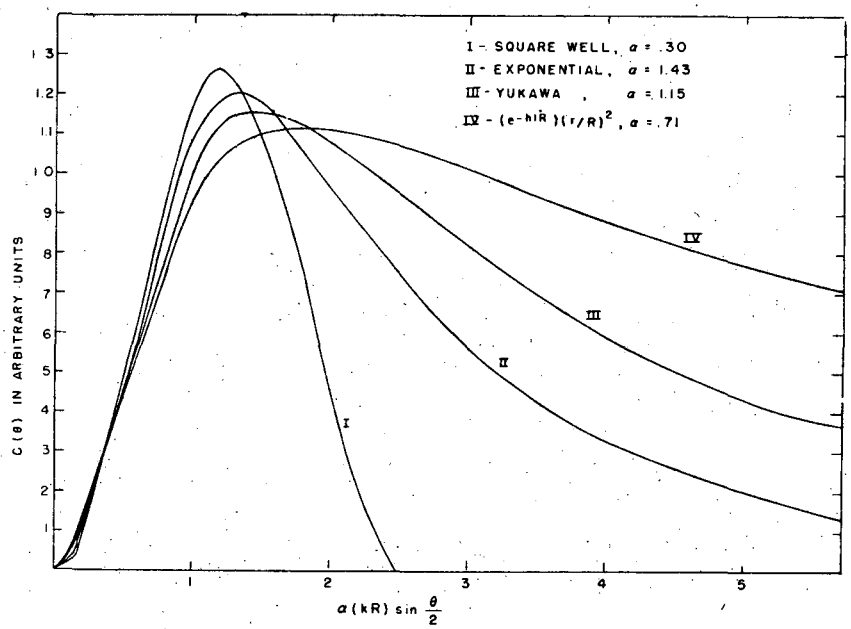
I - SQUARE WELL, $\alpha = .30$
II - EXPONENTIAL, $\alpha = 1.43$
III - YUKAWA, $\alpha = 1.15$
IV - $(e^{-\alpha R})(r/R)^2$, $\alpha = .71$
C(θ) IN ARBITRARY UNITS
$\alpha(kR)\sin\frac{\theta}{2}$

Fig. 32

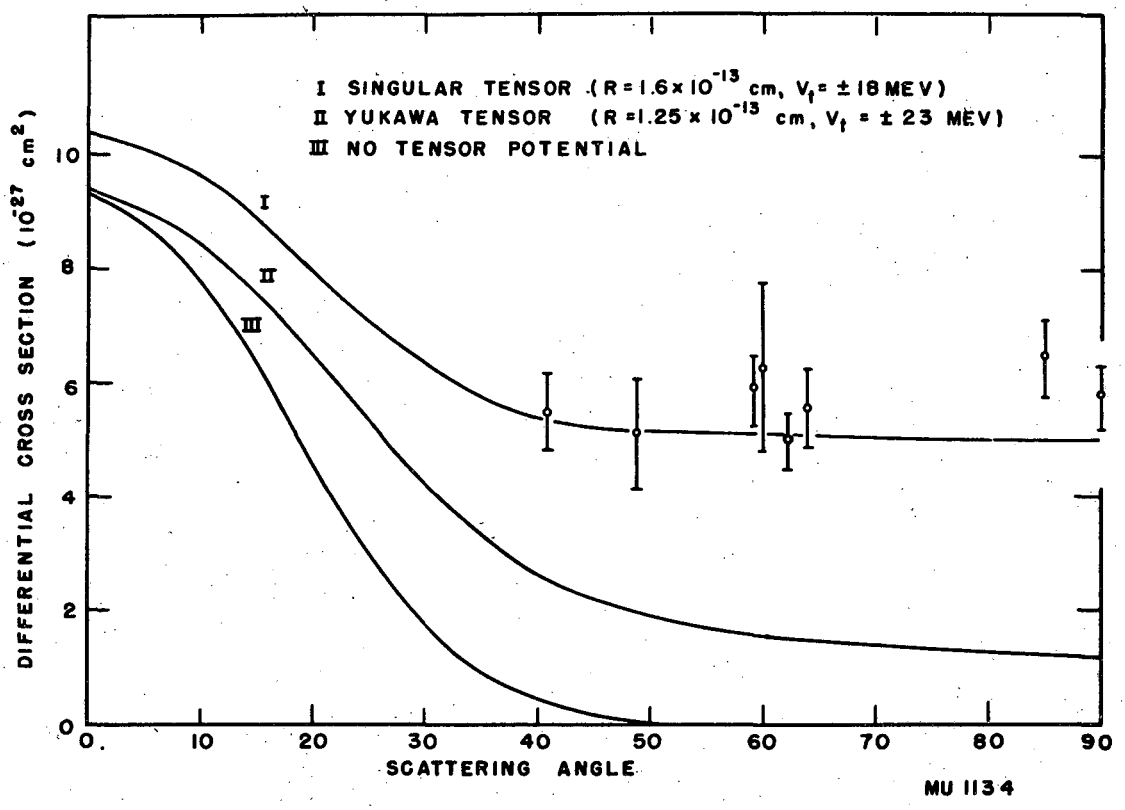
I SINGULAR TENSOR (R = 1.6 x 10^-13 cm, V_t = ± 18 MEV)
II YUKAWA TENSOR (R = 1.25 x 10^-13 cm, V_t = ± 23 MEV)
III NO TENSOR POTENTIAL
I
II
III
DIFFERENTIAL CROSS SECTION (10^-27 cm^2)
0
2
4
6
8
10
0.
10
20
30
40
50
60
70
80
90
SCATTERING ANGLE
MU 1134

Fig. 33